PRESSURE SOLUTION, POROSITY REDUCTION, AND TRANSPORT IN ROCKS

A DISSERTATION

SUBMITTED TO THE DEPARTMENT OF GEOPHYSICS

AND THE COMMITTEE ON GRADUATE STUDIES

OF STANFORD UNIVERSITY

IN PARTIAL FULFILLMENT OF THE REQUIREMENTS

FOR THE DEGREE OF

DOCTOR OF PHILOSOPHY

By

Doron Galmudi

February, 1998

CONTENTS

Abstract

1 Introduction **1**

1.1 General Introduction 1
1.2 Description of Chapters 1
1.3 References 3

2 Stability Analysis of a Pressure Solution Surface **4**

2.1 Abstract 4
2.2 Introduction 4
2.3 Elastic Analysis 5
2.4 Kinetics 8
2.5 Discussion of Results 12
2.6 Geological Implications 12
2.7 Conclusions 13
2.8 Acknowledgments 13
2.9 References 14

3 Elastic Strain Energy as a Control in the Evolution of Asymmetric Pressure Solution Contacts **17**

3.1 Abstract 17
3.2 Introduction 17
3.3 Mechanism 18
3.4 Discussion 21
3.5 Acknowledgments 23
3.6 References 24
3.7 Appendix: Full Solution of Diffusion Equation 25

4 Growth and Propagation of Stylolites **26**

4.1 Abstract 26
4.2 Introduction 26
4.3 Stylolites: Nucleation and Propagation 28
4.4 Computational Method and Assumptions 30
4.5 Results 31
4.5.1 General 32
4.5.2 Effect of Surface Energy 33
4.5.3 Effect of Solubility Difference 34
4.5.4 Effect of Elastic Moduli Difference 34
4.6 Conclusions 35
4.7 Acknowledgments 35
4.8 References 36

5 A Physical Model for Porosity Reduction in Sandstones **37**

5.1 Abstract 37
5.2 Introduction 37
5.3 Elastic Models and Pore-Space Topology 39
5.4 Modified Upper Hashin-Shtrikman Bound 40
5.5 Permeability Model and Data 43
5.6 Formation Factor 45
5.7 Conclusions 47
5.8 Acknowledgments 47
5.9 References 48
5.10 Appendix: Comparing the MUHS Curves to Experimental Data for Sintered Glass Beads 49

6 Permeability in Clean and Shaly Sandstones **50**

6.1 Abstract 50
6.2 Introduction 51
6.3 Permeability Model for Clean Sandstones 51
6.4 Permeability Model for Shaly Sandstones 54
6.5 Results 55
6.6 Conclusions 59
6.7 Acknowledgments 59
6.8 References 60

7 Stresses in Anisotropic Cylinders **61**

7.1 Introduction 61
7.2 Analysis 61
7.3 Acknowledgments 66
7.4 References 67

Appendix: Simulations of Stylolite Growth **68**

A.1 Overview 68
A.2 Similar properties 69
A.3 No surface energy 71
A.4 Different solubilities 73
A.5 Different elastic moduli 75

ABSTRACT

Pressure solution, which has long been a very active area of research in the earth sciences, is one of the principal deformation mechanisms in crustal rocks, and it is often responsible for the dissolution and removal of huge volumes of rock. It causes porosity loss through compaction and cementation, fluid migration on scales up to that of tectonic basins, and is a major influence on reservoir structure at depth. Still, many aspects of the pressure solution process remain unexplained. Stylolites are a long-standing puzzle in pressure solution research. In the first part of this thesis, I develop a theoretical description of their initiation and growth. I suggest that a stylolite forms as an elastic-energy driven instability on a pressure solution surface, when the maximum principal stress is very much greater than the other principal stresses. Linear stability analysis shows, that the wavelength of the instability is determined by the relative values of the effective principal stresses, by the surface energy of the rock or mineral, and by the active transport mechanism. Next, I show that a small solubility difference between two surfaces, that come together to form a pressure solution surface, can cause only one surface (the slightly more soluble one) to dissolve, while leaving the other almost unaffected. This is facilitated by diffusive coupling between the two surfaces; the fluid at the thin contact is very close to saturation, therefore, the small extra amount dissolved from the slightly more soluble surface, can easily diffuse across to the other surface, and fully saturate the adjacent fluid layer, thus severely inhibiting its dissolution. This result explains the relatively large relief of stylolites, as well as another previously unexplained pressure solution phenomenon: pitted pebbles. Next, these theoretical results are incorporated into a computer simulation of stylolite growth and propagation. It is shown that within the stress domains predicted by the linear stability analysis, a small initial perturbation of a pressure solution surface will grow in amplitude, and propagate along the surface, provided the elastic energy driving the instability can overcome the resultant increase in surface energy.

In the second part of this thesis, I study the effects of pore-space microstructure on fluid permeability, and acoustic velocities in sandstones. I derive porosity-velocity, porosity-permeability, and porosity-formation factor relationships in clean sandstones, by making the simplifying assumption of uniform porosity reduction (UPR), and by using the concept of effective porosity. UPR means that, in a sandstone, the pore shapes remain essentially constant as porosity is reduced by diagenesis. Effective porosity is the well-connected part of the pore-space, which serves to transmit fluid. All formulas match the data well, and the formulas that relate porosity to permeability and formation factor, agree

better with experimental Fontainebleau sandstone data, than the established forms of the Kozeny-Carman equation, and Archie's law. Next, I extend the UPR and effective porosity concepts, by employing them, in conjunction with three-dimensional network modeling, to explain systematic scatter in Fontainebleau porosity-permeability data. The modeling suggests that this scatter is a result of an increasing variability in tortuosity at small effective porosities. Finally, the model is modified to include clay in the pore-space, and I use it to derive formulas that give high and low permeability estimates, using porosity, clay content, and grain size as input. The equations are then successfully tested on a set of 72 shaly sandstones, and I find that the measured permeabilities almost always fall between the two estimates. The log-average, of the high and low estimates, predicts the measured permeability of all the data, to within an order of magnitude.

In the final chapter of the thesis I explore the applicability of the Saint-Venant principle to cylindrically anisotropic bodies. Axisymmetrical stresses in an infinitely long hollow isotropic circular cylinder (plane strain) quickly approach their asymptotic values as the external radius increases. This is not the case if the cylinder is even slightly anisotropic -- asymptotic solutions (for an infinitely large external radius) do not exist. I show that if the cylinder is stiffer in the radial direction than in the tangential direction, the internal stresses increase infinitely with increasing external radius. If, on the other hand, the cylinder is stiffer in the tangential direction than in the radial direction, then at any fixed point inside the cylinder, the stresses approach zero as the outer radius increases.

CHAPTER 1

INTRODUCTION

General

Pressure solution is an extremely important deformation mechanism in crustal rocks. In many geological settings, it is responsible for the dissolution and removal of huge volumes of rock, resulting in porosity loss through compaction and cementation, fluid migration on a variety of scales -- up to that of tectonic basins (Trurnit, 1968), and in the formation of a variety of geological features. The physical concept of pressure solution, that subjecting a mineral to stress enhances its solubility, has been recognized now for well over a century (Thompson, 1862), yet, some of the most important aspects of this process remain unexplained. Stylolites, which are geometrically irregular pressure solution surfaces, are an example of a persistent area of controversy in pressure solution research. The first part of my thesis is dedicated to developing a theoretical description of their initiation and growth.

In the second part of this thesis, I study the effects of pore-space microstructure on fluid permeability, and acoustic velocities in sandstones. The idea behind this work is, that as a rock evolves, through cementation, clay deposition, pressure solution, and other geological processes, some of the characteristics of its pore-space are maintained. I use this concept to develop a set of models that relate the porosity of a rock, to its acoustic and transport properties.

Finally, I consider the elastic problem of a cylindrically anisotropic body subjected to external loading. The results are closely related to the decay of boundary conditions and, in general, to the problem of applicability of Saint-Venant's principle to anisotropic solids.

Description of Chapters

Chapter 2, suggests that stylolites form as a morphological instability of a pressure solution surface. The instability is driven by the elastic strain energy, and resisted by the surface energy. Using linear stability analysis, I demonstrate that a pressure solution surface becomes unstable if the stress tangential to it is greater, or else, if it is much smaller, than the normal stress. The latter condition applies to the formation of stylolites, and the instability wavelength is related to the stress state, the surface energy, and the active transport mechanism. Therefore, it may, in the future, be possible to relate stylolite

morphology to the three-dimensional paleo-stress field. This work was done together with Amos Nur and Einat Aharonov.

In Chapter 3, I study diffusive coupling between two similar surfaces that come together to form a pressure solution contact. The total amount of material dissolved depends on the normal stress. However, I show that if the contact is sufficiently thin, a very small solubility difference between the two surfaces, can result in very asymmetric dissolution. The slightly more soluble surface dissolves, while the less soluble surface remains almost unaffected. This result explains the often large relief of stylolites, and the occurrence of pitted pebbles, which are another, previously unexplained, pressure-solution related phenomenon. The work presented in this chapter was done in collaboration with Amos Nur.

Chapter 4 brings together, and applies, the theory developed in Chapters 2 and 3, to a computer simulation of stylolite propagation and growth. Using a finite element code, I compute the stress field of a pressure solution contact, that has a small initial heterogeneity. The results are employed to calculate the dissolution at each point along the contact, the geometry is then altered accordingly, and the steps repeated. The simulation results confirm the major conclusions of the linear stability analysis, and they show that as a stylolite grows in amplitude, it also propagates along the pressure solution seam. Finally, I test the effect of different parameters, such as solubility, surface energy, and elastic moduli, on the morphology of the simulated stylolite. Amos Nur worked with me on this research.

In Chapter 5, I show that porosity-velocity, porosity-permeability, and porosity-formation factor relationships in clean sandstones, can be easily predicted, if: a) one assumes that pores in the rock shrink uniformly, and b) the effective porosity is related to transport properties instead of the total porosity. The formulas that relate porosity to permeability and formation factor, agree better with experimental Fontainebleau sandstone data, than the established forms of the Kozeny-Carman formula, and Archie's law. Jack Dvorkin and Amos Nur helped me with the work presented in this chapter.

Chapter 6 extends the uniform porosity reduction (UPR) and effective porosity concepts, by using them in conjunction with three-dimensional network modeling, to explain a systematic scatter in Fontainebleau porosity-permeability data. The modeling suggests that this scatter is a result of an increased variability in tortuosity at low effective porosities. The model is then modified to include clay in the pore-space, allowing me to derive formulas that give high and low permeability estimates for a set of 72 shaly sandstones (using porosity, clay content, and grain size as input). The measurements almost always fall between the proposed estimates, and their log-average predicts the

permeability of almost all data to within an order of magnitude. It also predicts the permeabilities somewhat better than other, well established methods, that require more input. Amos Nur and Jack Dvorkin worked with me on this research.

Chapter 7 addresses the important problem of the applicability of the Saint-Venant principle to anisotropic bodies. I show that if a cylinder, that is subjected to external loading, is stiffer in the radial direction than in the tangential direction, the internal stresses actually increase away from the loaded boundary. If, on the other hand, the cylinder is stiffer in the tangential direction than in the radial direction, then the stresses decay rapidly away from the boundary. Jack Dvorkin and Amos Nur helped me with this work.

REFERENCES

Thompson, J., 1862, On crystallization and liquefaction, as influenced by stresses tending to change of form in the crystals: Proc. Roy. Soc. London, **11**, 473-481.

Trurnit, P, 1968, Pressure solution phenomena in detrital rock: Sedim. Geol., **2**, 89-114.

CHAPTER 2

STABILITY ANALYSIS OF A PRESSURE SOLUTION SURFACE

ABSTRACT

I present a linear stability analysis of a pressure solution surface subjected to a non-hydrostatic stress field. A small sinusoidal perturbation is imposed on an initially flat solid/fluid interface, and the consequent changes in elastic strain energy and in surface energy are calculated. The results demonstrate that if the far-field lateral stresses are either greater, or much smaller than the fluid pressure, the perturbed configuration has a lower strain energy than the initial one. For wavelengths greater than a critical wavelength this energy decrease may be large enough to offset the increased surface energy. Under these conditions, the perturbation will grow unstably. If these conditions are not met, the surface becomes flat. The growth rate and the wavelength of the maximally unstable mode depend on the mechanism of matter transport. I calculate the growth rate for the case where diffusion along the interface is rate limiting, and determine the maximally unstable wavelength, i.e., the wavelength that will grow fastest. The instability discussed in this chapter may account for the formation of stylolites, as well as other pressure solution phenomena, such as roughening of grain contacts and phase-change boundaries.

INTRODUCTION

Pressure solution is a very important deformation mechanism in crustal rocks. It may result in strains greater than 50% and in a variety of geologic features such as stylolites, pitted pebbles, slip cleavages, marl-limestone alterations, and sutured grain contacts (Stockdale, 1922; Alvarez et al., 1978; Robin, 1978; Englender, 1981; Gratier, 1983; Ricken, 1986). Several researchers have shown that the pressure solution mechanism can also be activated and studied in the laboratory (Sprunt and Nur, 1977; Rutter, 1983; Urai, 1985; Gratier and Guiguet, 1986; Tada and Siever, 1986; Spiers and Schutjens, 1990; Hickman and Evans, 1991, 1992). The physical concept of pressure solution, that subjecting a mineral to stress enhances its solubility, has been recognized now for well over a century (Thompson, 1862; Sorby, 1863). However, despite a vast amount of research, it has so far proved very hard to develop an adequate understanding of this process. Difficulties arise because pressure solution involves phase transformation and material transport in stress fields and geometries that change with time and are often very

complicated. More recent theoretical progress in the thermodynamics of non-hydrostatically stressed solid-fluid interfaces (e.g., Paterson, 1973; Green, 1984; Lehner and Bataille, 1985; Heidug, 1991; Heidug and Leroy, 1994; Leroy and Heidug, 1994) provides the tools and insight to resolve many of these problems. Still, some of the most fundamental mechanisms and phenomena associated with pressure solution remain unexplained.

Stylolites are among the least well-explained of all pressure solution phenomena. Although mechanisms have been proposed that account for them as a manifestation of pressure solution localization (e.g. Ortoleva et al., 1987; Merino et al. 1983; Dewers and Ortoleva, 1990), no satisfactory explanation has been given for their characteristic irregular geometry. In this chapter, I lay a foundation for understanding the nucleation and growth of stylolites, by analyzing the stability of a stressed pressure solution surface. This is done by imposing a small sinusoidal perturbation on an initially flat solid/fluid interface that is subjected to stress. Assuming that no work is exchanged with the environment, the energy variation caused by this perturbation consists of a: a change in the elastic strain energy of the solid, and b: a change in the free surface energy. If the system has thereby achieved a lower energy state, the perturbation will grow, otherwise it decays and the interface becomes flat. The analysis shows that growth can occur only for perturbation wavelengths greater than a critical wavelength, which is determined by both the stress state and the surface energy value. The rate of the growth or decay depends also on the manner of matter transport, e.g. diffusion along an interfacial film, or dissolution/precipitation into the bulk fluid. The proposed instability may play an important role in other geological processes such as roughening of grain boundaries and fracture surfaces. More generally, it may apply to any phase transformation or reaction at a stressed interface where at least one of the phases is elastic. The analysis also suggests that the morphology of the instability may be determined by the stress, and conversely, the stress may be deduced from the morphology.

ELASTIC ANALYSIS

In this section, as well as the next, I follow the procedure used by Srolovitz (1989) to analyze the stability of laterally stressed thin films. The analysis is generalized by allowing the surface to be in contact with a fluid that has non-zero pressure. To determine the effect of surface evolution on the elastic stresses in the solid, let us consider an initially flat solid slab, lying on the $x-z$ plane, and constrained in the z direction (Figure 1). I induce a

state of uniform biaxial stress in the slab by applying a lateral stress P_l at $x = 0,l$, and by exposing the solid to fluid at pressure P_v at $y = 0$. The resulting strains are:

$$\varepsilon_{xx} = \frac{\left(1-\nu^2\right)}{E} P_l - \frac{\nu(1+\nu)}{E} P_v$$

$$\varepsilon_{yy} = \frac{\left(1-\nu^2\right)}{E} P_v - \frac{\nu(1+\nu)}{E} P_l \tag{1}$$

where E and ν are the Young's modulus and Poisson ratio. The elastic strain energy is

$$u_e = \frac{(1-\nu^2)}{2E}\left[P_l^2 + P_v^2 - \frac{2\nu}{1-\nu} P_l P_v\right]. \tag{2}$$

Next, we assume that the solid/fluid interface obtains a small-amplitude sinusoidal profile

$$h(x) = H\sin(kx), \tag{3}$$

such that $Hk << 1$. The stress field in the solid is a superposition of a hydrostatic and a deviatoric component. To calculate the deviatoric stress, we search for an Airy stress function of the form

$$\tilde{\Phi} = \frac{(P_l - P_v)y^2}{2} + \sum_{n=1}^{\infty}(A_n + B_n y)e^{-nky}\sin(nkx), \tag{4}$$

where A_n and B_n are constants that can be determined from boundary conditions. Since we are assuming that $Hk << 1$, only the first term of the infinite series in equation (4) has to be considered. The deviatoric stress components can then be written,

$$\tilde{\sigma}_{xx} = \partial^2\tilde{\Phi}/\partial y^2 = (P_l - P_v) - k\left[2B - k(A + By)\right]e^{-ky}\sin(kx),$$

$$\tilde{\sigma}_{yy} = \partial^2\tilde{\Phi}/\partial x^2 = -k^2(A + By)e^{-ky}\sin(kx),$$

$$\tilde{\sigma}_{xy} = -\partial^2\tilde{\Phi}/\partial x\partial y = -k\left[B - k(A + By)\right]e^{-ky}\cos(kx). \tag{5}$$

The components of the deviatoric stress that are normal and tangential to the interface are given by

$$\tilde{\sigma}_{nn} = \tilde{\sigma}_{xx}\sin^2\alpha + \tilde{\sigma}_{yy}\cos^2\alpha - 2\tilde{\sigma}_{xy}\sin\alpha\cos\alpha,$$

$$\tilde{\sigma}_{\tau\tau} = \tilde{\sigma}_{xx}\cos^2\alpha + \tilde{\sigma}_{yy}\sin^2\alpha + 2\tilde{\sigma}_{xy}\sin\alpha\cos\alpha,$$

$$\tilde{\sigma}_{\tau n} = \left(\tilde{\sigma}_{yy} - \tilde{\sigma}_{xx}\right)\sin\alpha\cos\alpha + \tilde{\sigma}_{xy}\left(\cos^2\alpha - \sin^2\alpha\right), \tag{6}$$

where $\alpha = \tan^{-1}\left(\partial h/\partial x\right)$. The deviatoric stresses $\tilde{\sigma}_{nn}$ and $\tilde{\sigma}_{\tau n}$ must vanish at the solid/fluid boundary. Therefore, assuming again that $Hk << 1$, we obtain

$$A = 0 \text{ and } B = -\left(P_l - P_v\right)H. \tag{7}$$

Adding the hydrostatic component, and again using the small amplitude assumption, we find that along the interface, to first order in Hk

$$\sigma_{\tau\tau} = P_l + 2\left(P_l - P_v\right)Hk\sin(kx),$$

$$\sigma_{nn} = Pv, \quad \sigma_{\tau n} = 0. \tag{8}$$

Therefore, the change in elastic energy at the solid/fluid boundary resulting from the perturbation imposed on the surface is

$$\delta u_e = \frac{2(1-\nu^2)}{E}\left(P_l - P_v\right)\left(P_l - \frac{\nu}{1-\nu}P_v\right)Hk\sin(kx) \tag{9}$$

To maintain the constant stress boundary condition at $x = 0,l$, some work must be done by or on the system, however this work term is second order in Hk, and can be left out of the present discussion.

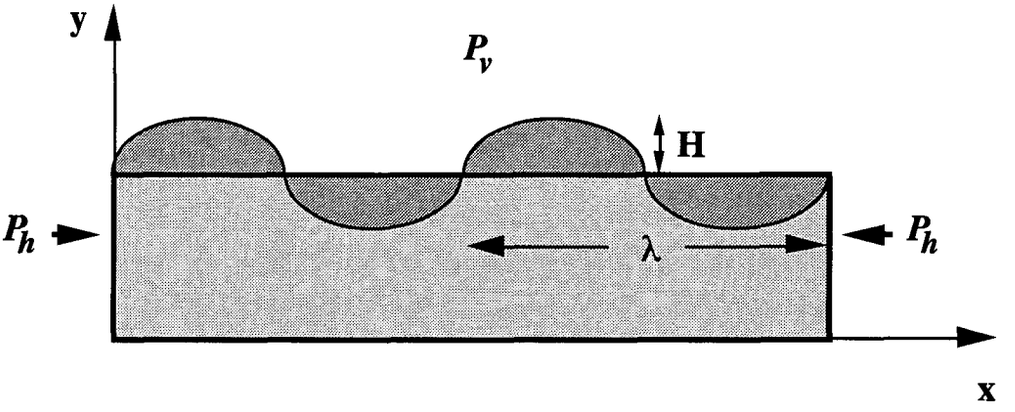

Figure 1: A small sinusoidal perturbation is imposed on an initially flat surface that is subjected to lateral stress, P_l and fluid pressure P_v.

KINETICS

The chemical potential at the boundary can be written as (Asaro and Tiller, 1972)

$$\mu(s) = \mu_0 + \Omega\left(\gamma\kappa(s) + u_e - P_v\right). \tag{10}$$

Here s is the coordinate along the solid/fluid interface, μ_0 is the chemical potential of a reference flat interface, Ω the atomic volume, γ the interfacial energy density, and the curvature κ is defined as

$$\kappa = -\partial^2 h/\partial x^2\left[1+\left(\partial h/\partial x\right)^2\right]^{-3/2}. \tag{11}$$

Unless the fluid pressure is negligible compared to the other stresses acting on the system, $\sigma_{nn}\Omega$ is much larger than $u_e\Omega$, and therefore the latter term is often neglected in theoretical analyses. However, we are interested in the chemical potential difference driving the instability, which is the chemical potential difference between the flat and the wavy surface configurations. In this case the $\sigma_{nn}\Omega$ term cancels out because σ_{nn} is constant at the solid/fluid interface. Note also that the total amount of work the solid surface exchanges with the fluid is the same for the flat and the wavy cases because of the geometrical symmetry of the perturbation. The chemical potential difference driving the instability can therefore be reduced to

$$\delta\mu(s) = \Omega\left(\gamma\kappa(s) + \delta u_e\right) \tag{12}$$

If diffusion is the rate determining step, we use the Nernst-Einstein equation:

$$V = -\frac{D}{\rho T}\frac{\partial\mu}{\partial s}. \tag{13}$$

Here V is the atomic diffusion velocity along the interface, D is the interface diffusivity, and ρT is the thermal energy (ρ is Boltzmann's constant). The resulting change rate of profile is (Mullins, 1957)

$$\frac{\partial h}{\partial t} = -\frac{D\Omega\beta}{\rho T}\frac{\partial^2\mu}{\partial s^2}, \tag{14}$$

where β is the number of atoms per unit area. By substituting equation (9) into equation (12), and eliminating terms in κ that are second order in Hk we find that

$$\delta\mu = \left[\frac{2(1-\nu^2)}{E}\left(P_l - P_v\right)\left(P_l - \frac{\nu}{1-\nu}P_v\right) - \gamma k\right]\Omega Hk\sin(kx). \tag{15}$$

To first order in Hk, $ds = dx$, therefore substitution of equation (15) into equation (14) yields

$$\left(\frac{\partial h}{\partial t}\right) = \left[\frac{2(1-\nu^2)}{E}\left(P_l - P_v\right)\left(P_l - \frac{\nu}{1-\nu}P_v\right) - \gamma k\right]\Omega^2 Hk^3 \sin(kx). \qquad (16)$$

Finally, by combining equations (3) and (16), we find that for a short time the sinusoidal perturbation amplitude will grow as $\exp(\psi t)$ where

$$\psi = \left[\frac{2(1-\nu^2)}{E}\left(P_l - P_v\right)\left(P_l - \frac{\nu}{1-\nu}P_v\right) - \gamma k\right]\left(\frac{D\Omega^2\beta}{\rho T}\right)k^3. \qquad (17)$$

To calculate the critical wavelength, λ_0, we simply set $\Psi = 0$, and obtain

$$\lambda_0 = \frac{\pi E\gamma}{(1-\nu^2)}\left[\left(P_l - P_v\right)\left(P_l - \frac{\nu}{1-\nu}P_v\right)\right]^{-1}. \qquad (18)$$

A sinusoidal perturbation whose wavelength is smaller than λ_0 will be smoothed out by diffusion along the interface. If the perturbation wavelength is greater than λ_0, diffusion will allow it to grow. It is interesting to note that if $P_v \geq P_l \geq (\nu/1-\nu)P_v$, there will be no growth irrespective of the value of γ. The reason is that for these stress-states, the elastic strain energy at the perturbation troughs is smaller than at the crests. The growth exponent ψ has a maximum for $\lambda_{max} = 4\lambda_0/3$, therefore a perturbation with this wavelength will grow fastest . These results are summarized in Figure 2, where I used numerical values that are typical for a quartz-water system at $300°C$: $D = 10^{-9} m^2/s$, $\Omega = 2.3 \times 10^{-5} m^3/mol$, $E = 0.8 \times 10^{11} N/m^2$, $\nu = 0.1$, and $\gamma = 0.5 J/m^2$ (Holland and Malinin, 1979; Lehner and Bataille, 1985). If dissolution/precipitation is the rate determining step it can be shown (Srolovitz, 1989) that λ_0 remains the same as in the diffusion-controlled case, but now $\lambda_{max} = 2\lambda_0$.

In this section, I have calculated the kinetics for the fundamental case of a stressed solid surface in contact with its own solution. It was assumed that diffusion takes place

predominantly along the solid/fluid interface. This assumption is valid if, for example, the fluid layer is very thick compared to the wavelength of the perturbation, or if it is very thin and not in contact with any other sources and sinks of material. Let us consider a simple model of a stylolite, where a thin fluid layer separates two solid-fluid interfaces. In that case, the thermodynamic force driving the instability is the same as the one in the single-interface system I analyzed, and therefore λ_0 is the same too. However, the kinetics are now different because diffusion can also take place across the fluid layer, therefore λ_{max} is different.

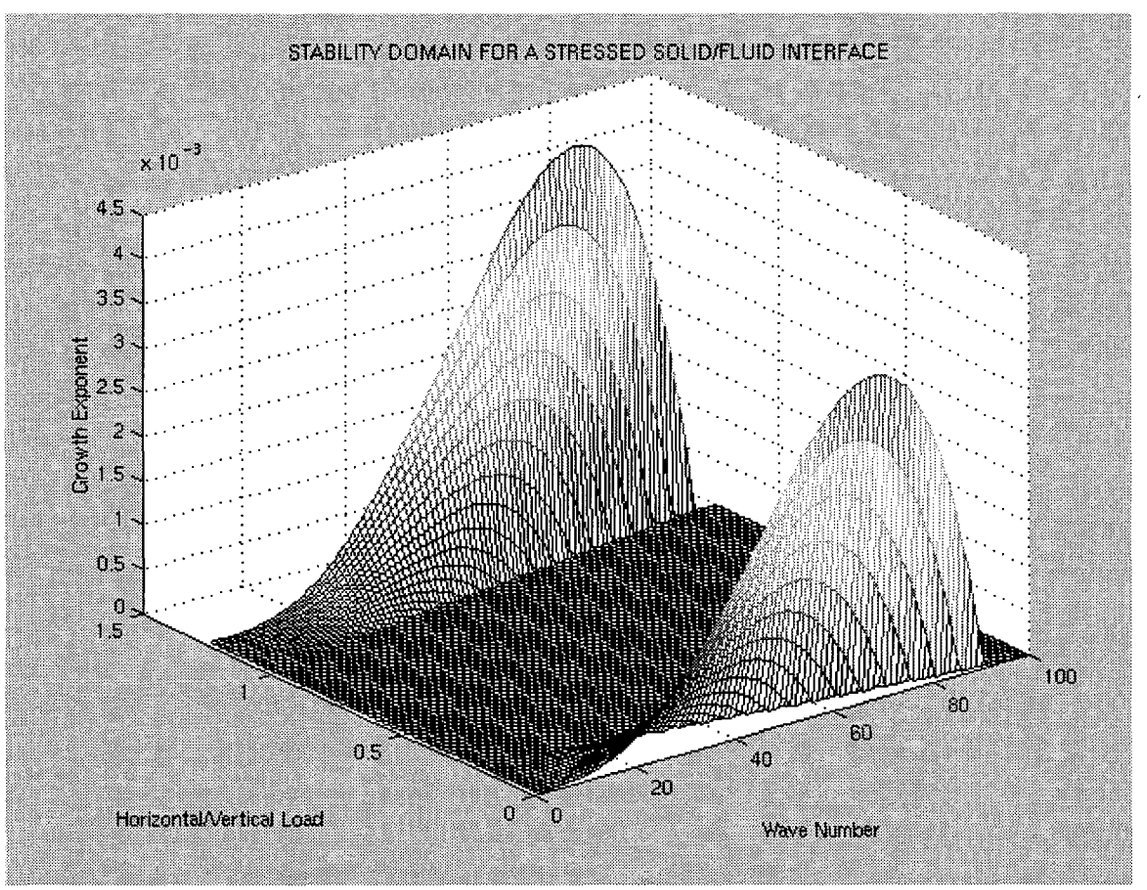

Figure 2: Two instability domains for a stressed solid/fluid interface: the first is when the horizontal stress is greater than the vertical stress, and the second is when it is very small compared to the vertical stress. Surface energy establishes a cutoff for short wave-lengths. The vertical load in this example is $10MPa$, and k is in m^{-1}. Negative values of growth exponent (i.e. perturbation decays) are omitted.

DISCUSSION OF RESULTS

The evolution of the perturbed surface is dictated by a competition between the elastic strain energy and the free surface energy of the system. When $P_l > P_v$ (the first instability mode), the strain energy is greatest at the "troughs" and least at the "crests" of the sinusoidal perturbation (Fig. 1). This will cause the instability to grow provided that the driving forces overcome the surface tension. To illustrate the second mode of instability, let us consider simple case where $P_v > 0$, $P_l = 0$. The fluid pressure is everywhere normal to the surface, and therefore it has a component that tends to squeeze the crests, and pull apart the troughs of the perturbed surface. Superposed on the general state of Poisson extension of the solid, this leads to greater extension at the troughs than at the crests, and again the perturbation grows, provided that the driving forces are strong enough to overcome the surface tension. When superposed on a general state of compression (e.g., when P_v is only slightly larger than P_l), the extra amount of compression at the crests and extension in the troughs leads to greater strain energy at the crests than at the troughs, and the perturbation decays.

GEOLOGICAL IMPLICATIONS

A well-known and often used model for a pressure solution contact is the one proposed by Weyl (1959), where a thin continuous water film is assumed to exist between the two solid surfaces. For the system to be mechanically stable, this film must be able to support shear stresses (Rutter, 1983), so it is believed that this water is strongly adsorbed to the mineral surfaces or, in some instances, to the surface of an intervening clay layer. Because the analysis presented in this chapter assumes that the fluid phase is free and unstructured, care must be taken in directly applying its results to this type of interface. However, I believe that the type of instability described for the case $P_l/P_v < (\nu/1-\nu)$ is the one driving stylolite and microstylolite growth. I suggest that under these conditions of stress, i.e. a minimum principal stress that is much smaller than the maximum principal stress, stylolites may develop. If P_l/P_v is larger, the pressure solution surface remains flat. These conclusions are consistent with tension gashes that are often associated with stylolite seams, and tend to be perpendicular to them (Bushinskiy, 1961; Fletcher and Pollard, 1983; Raynaud and Carrio-Schaffhauser, 1992). I have also run numerical simulations on models where a thin interface layer is allowed to have non-zero shear strength (work in progress), and found that interface perturbations grow unstably, provided that P_l/P_v is small. Other types of geological phenomena may result from the interface instability for the

stress-states where $P_l/P_v > 1$. This instability may, for example, increase surface roughness in grain and fracture surfaces undergoing pressure solution, and also affect the morphology of surfaces where a stress-sensitive reaction or phase change are taking place, and at least one of the phases is elastic.

CONCLUSIONS

I have analyzed the stability of a pressure solution surface subjected to a non-hydrostatic stress field by imposing a small sinusoidal perturbation on an initially flat solid/fluid interface. If the far-field lateral stresses are either greater, or much smaller than the fluid pressure, the perturbed configuration has a lower strain energy than the initial one. For wavelengths greater than a critical wavelength this energy decrease may be large enough to offset the increased surface energy. If these conditions are met, then the perturbation will grow unstably. If they are not, the surface will become flat. I have also derived the growth rate for the case where diffusion along the interface is rate limiting, and determined the maximally unstable wavelength, i.e. the wavelength that will grow fastest. I believe that this instability may account for the formation of stylolites and other pressure solution phenomena, such as roughening of grain contacts and phase-change boundaries.

ACKNOWLEDGEMENTS

The work presented in this chapter, was done in collaboration with Amos Nur and Einat Aharonov, and supported by the SRB.

REFERENCES

Alvarez, W., Englender, T., and Geiser, P.E., 1978, Classification of solution cleavage in pelagic limestones: Geology, **6**, 263-266.

Asaro, R.J., and Tiller, W.A., 1972, Interface morphology development during stress corrosion cracking: Part I, via surface diffusion: Met. Trans., **3**, 1789-1796.

Barber, J.R., 1992, Elasticity: Dordrecht; Klunwer Academic Publishers

Bushinskiy, G.I., 1961, Stylolites: Jzv. Akad. Nauk. S.S.S.R., Ser. Geol. **8**, 31-46.

Dewers, T. and Ortoleva, P., 1990, A coupled reaction/transport/mechanical model for intergranular pressure solution, stylolites, and differential compaction and cementation in clean sandstones: Geochim. et Cosmochim. Acta, **54**, 1609-1625.

Englender, T., and Geiser, P.E., and Alvarez, W., 1981, Role of pressure solution and dissolution in geology: Geology, **9**, 44-45.

Fletcher, R.C., and Pollard, D.D., 1981, Anticrack model for pressure solution surfaces: Geology, **9**, 419-424.

Gratier, J.P., 1983, Estimation of volume changes by comparative chemical analyses in heterogeneously deformed rock (folds with mass transfer): J. Struct. Geol., **5**, 329-339.

Gratier, J.P., and Guiguet, R., 1986, Experimental pressure-solution deposition on quartz grains: the crucial effect of the nature of the fluid: J. Struct. Geol., **8**, 845-856.

Green, H.W., 1984, Pressure solution creep: Some causes and mechanisms: Journal of Geophysical Research, **89**, 4313-4318.

Heidug, W.K., 1991, A thermodynamic analysis of the conditions of equilibrium at nonhydrostatically stressed and curved phase boundaries: Journal of Geophysical Research, **96**, 909-921.

Heidug, W.K., and Leroy, Y.M., 1994, Geometrical evolution of stressed and curved solid-fluid boundaries, 1, Transformation kinetics: Journal of Geophysical Research, **99**, 505-515.

Hickman, S., and Evans, B., 1991, Experimental pressure solution in halite: the effect of grain/interphase boundary structure: J. Geol. Soc. London, **148**, 549-560.

Hickman, S., and Evans, B., 1992, Growth of grain contacts in halite by solution transfer: implications for diagenesis, lithification, and strength recovery: in Fault Mechanics and Transport Properties of Rocks, B. Evans and T.F. Wong (eds.), Academic Press, 253-280.

Holland, H.D., and Malinin, S.D., 1979, The Solubility and Occurrence of Non-Ore Minerals; Geochemistry of Hydrothermal Ore Deposits, 2nd Edition, edited by H.L. Barnes (J. Wiley & Sons, New York), 461-508.

Leroy, Y.M., and Heidug, W.K., 1994, Geometrical evolution of stressed and curved solid-fluid phase boundaries, 2, Stability of cylindrical pores: Journal of Geophysical Research, **99**, 517-530.

Lehner, F.K., and Bataille, J., 1985, Non-equilibrium thermodynamics of pressure solution: Pure Appl. Geoph., **122**, 53-85.

Merino, E., Ortoleva, P., and Strickholm, P., 1983, Generation of evenly-spaced pressure solution seams during (late) diagenesis: a kinetic theory: Contrib. Mineral. Petrol., **82**, 360-370.

Mullins, W.W., 1957, Theory of Thermal Grooving: J. of Appl. Physics, **28**, 333-339.

Ortoleva, P., Merino, E., Chadam, J., and Moore, C.H., 1987, Geochemical self organization. I: feedback mechanisms and modeling approach: Amer. J. Sci., **287**, 979-1002.

Paterson, M.S., 1973, Nonhydrostatic thermodynamics and its geologic implications: Rev. Geophys. Space Phys., **11**, 355-389.

Raynaud, S., and Carrio-Schaffhauser, E., 1992, Rock matrix structures in a zone influenced by a stylolite: J. Struct. Geol., **14**, 973-980.

Ricken, W., 1986. Diagenetic Bedding; Lecture notes in Earth Sciences, **6**, Springer-Verlag, Berlin, 210pp.

Robin, P.Y.F., 1978, Pressure solution at grain-to-grain contacts: Geochim. Cosmochim. Acta, **42**, 1383-1390.

Rutter, E.H., 1983, Pressure solution in nature, theory, and experiment: Geological Society of London Journal, **140**, 725-740.

Sorby, J.C., 1863, Uber kalkstein-gescheibe mit eindrucken: Neues Jahrb. Mineral. Geol. Paleontol., 801-807.

Spiers, C.J. and Schutjens, P.M.T.M., 1990, Densification of crystalline aggregates by fluid phase diffusional creep: Deformation Processes in Minerals, Barber, D.J. and Meredith, P.D. (eds.), Unwin Hyman, London, 334-353.

Sprunt, E.S., and Nur, A., 1977, Experimental studies of the effects of stress on solution rate: Journal of Geophysical Research, **82**, 3013-3022.

Srolovitz, D.J., 1989, On the stability of surfaces of stressed solids: Acta Metall., **37**, 621-625.

Stockdale, P.B., 1922, Stylolites: their nature and origin: Indiana Univ. Studies, **9**, 1-97.

Tada, R. and Siever, R., 1986, Experimental knife edge pressure solution of halite: Geochim. Cosmochim. Acta, **50**, 29-36.

Thompson, J., 1862, On crystallization and liquefaction, as influenced by stresses tending to change of form in the crystals: Proc. Roy. Soc. London, **11**, 473-481.

Urai, J.L., 1985, Water-enhanced dynamic recrystallization and solution transfer in experimentally deformed carnallite: Tectonophysics, **120**, 285-317.

Weyl, P.K., 1959, Pressure-solution and the force of crystallization -- a phenomenological theory: Journal of Geophysical Research, **64**, 2001-2025.

CHAPTER 3.

ELASTIC STRAIN ENERGY AS A CONTROL IN THE EVOLUTION OF ASYMMETRIC PRESSURE SOLUTION CONTACTS

ABSTRACT

Subjecting a water-rock system to load can enhance the rock solubility by (1) increasing normal pressure at the dissolving surface and (2) raising the elastic energy of the rock. For pressure-solution surfaces, such as grain contacts, solution seams, and stylolites, the pressure term in the chemical potential equation is orders of magnitude larger than the strain-energy term. Thus, the contribution of the strain energy to the overall solubility of the system is very small. Indeed, it is most often ignored. Still, I show that the elastic strain energy at a pressure-solution interface, can have a profound effect on the manner in which it evolves. The mechanism I propose is the following: inducing a discontinuity in elastic strain energy across a pressure solution interface (e.g., by changing its curvature) can cause one side to become slightly more soluble than the other. Part of the material that is thus dissolved may diffuse the short distance across the fluid layer and raise the saturation in the vicinity of the less-soluble surface. If the fluid layer was already close to saturation, the dissolution at the less-soluble surface may thus be severely slowed down or even halted. Therefore, although the strain-energy difference across the interface has a negligible effect on the total amount of material that is dissolved there, it may cause only one side to dissolve. In this way, the formation of stylolites can be facilitated by heterogeneities in the elastic-strain-energy difference along a pressure-solution interface.

INTRODUCTION

One of the most puzzling aspects of pressure solution, is that rock on one side of a dissolution interface commonly appears to have undergone extensive pressure solution, but the rock on the other side appears almost unaffected. A dramatic example is the occurrence of pitted pebbles, in which one pebble is penetrated by another, so that a deep dissolution depression is created in the "host" pebble, but the "guest" pebble does not undergo substantial dissolution itself (Trurnit, 1968). Stylolites also exhibit this type of behavior; column heights have been reported to be useful in many instances as estimators of the total thickness of material that has been removed at a pressure-solution interface (e.g., Delair

and Leroux, 1978). Such estimates imply that at least the highest columns have been relatively resistant to pressure solution; if not, the approach would significantly underestimate the total rock thickness dissolved. In fact, such concerns led to speculation that a new physical process, analogous to spontaneous polarization in ferromagnetism, was responsible for setting up "domains" along the stylolitic pressure-solution interface, in which dissolution occurs only on one side of the interface, or on the other (Guzzetta, 1984). However, no mechanism was offered.

To some extent, the differential dissolution across a pressure-solution interface can be accounted for by various means. An almost intact shell fragment at the top of the stylolite column may be inherently less soluble than the host rock; indeed it may have promoted the nucleation of a stylolite. Different strain energies in material on either side of a pressure-solution interface can also induce solubility differences. However, taken by themselves, these differences cannot account for the lopsidedness sometimes observed in nature, especially for those cases in which both sides of the interface have a similar composition.

To resolve this paradox, I propose the following mechanism: along a thin, water-permeated interface, where a small solubility difference exists between the two adjacent surfaces, solutes diffusing from the more soluble surface can inhibit, and even completely stop, the dissolution on the less soluble surface. Thus, despite the very small solubility difference, one side of the interface (the one with the greater elastic strain energy, for example) can do most, or all, of the dissolving while the other side is "shielded" from dissolution. In this chapter, I present a simple model to better understand the factors controlling this induced dissolution-shielding effect. The discussion will show that the proposed effect can, in principle, induce the type of polarization envisioned by Guzzetta (1984).

MECHANISM

In this section, I present a phenomenological model of solute diffusion at a pressure-solution contact. The motivation is to examine the effect of diffusive mass transfer within the contact region on the relative solubilities of the adjacent interfaces. Generally, the physical chemistry of surface processes is extremely complex, and it is a subject of extensive research. No attempt is made here to address many important issues that should be a part of any comprehensive model of a pressure-solution contact. My goal is simply to illustrate the proposed dissolution-shielding effect.

The tendency of a material to dissolve in a fluid is affected by the existing solute concentration. If one raises the solute concentration in that fluid, the dissolution slows

down until, at the saturation concentration, it stops. Additional increase in the saturation may cause precipitation to ensue. This behavior can be expressed by the relationship (Lasaga, 1981)

$$\frac{\partial c}{\partial n} = -\frac{h_0}{D}(c_s - c), \tag{1}$$

where n is the normal to the dissolving surface, c is the solute mass fraction in the fluid, c_s is the saturated mass fraction, h_0 is a mass transfer coefficient, and D is the diffusivity.

Let us now consider two identical parallel mineral surfaces on the x-z plane that extend to infinity in the z direction and are semi-infinite along the x axis (Fig. 1). The system is loaded with a compressive vertical stress, and the surfaces are separated by a thin water film. The vertical load is balanced by hydration forces, which are a consequence of a "structuring" of water molecules in the thin film (Israelachvili, 1991). We immerse this system in a large water reservoir where the background solute concentration is zero. Initially, the solute concentration in the water film is also zero. As the system approaches quasi-steady-state conditions, however, the solute concentration within the film increases because lateral diffusion in and out of the film is constrained by its thinness.

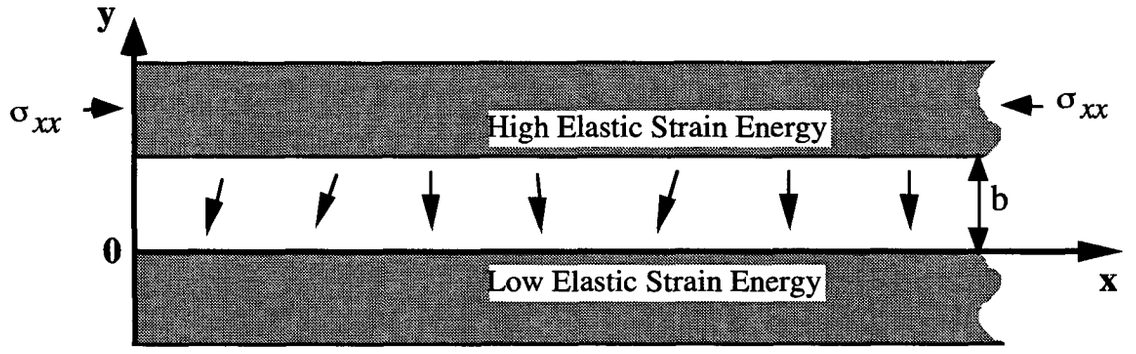

Figure 1: Diffusion across a pressure solution interface: applying lateral stress to the top surface causes material to go into solution and diffuse across the water film, raising the saturation at the unstressed surface, and inhibiting its dissolution.

Next, the top surface is loaded parallel to the x direction. Because the thin fluid film partially decouples non-normal tractions, the strain energy increases more on the top surface than on the bottom one. This strain-energy difference induces a solubility difference between the surfaces. As a result, extra material dissolves from the top surface,

and some of the resulting solutes diffuse towards the bottom surface and inhibit, to a degree, any dissolution that might be taking place there. To examine the effect of this mechanism on the quasi-steady-state behavior of the system, and how it is coupled to the overall diffusive flow, I solve the following diffusion problem:

$$\frac{\partial^2 c}{\partial x^2} + \frac{\partial^2 c}{\partial y^2} = 0,$$

$$\left.\frac{\partial c}{\partial y}\right|_{y=0} = -h\left(c - c_{s0}\right),$$

$$\left.\frac{\partial c}{\partial y}\right|_{y=b} = h\left(c - c_{sb}\right),$$

$$c|_{x=0} = 0,$$

$$\left.\frac{\partial c}{\partial x}\right|_{x\to\infty} = 0. \tag{2}$$

Here, c_{s0} and c_{sb} are the saturation concentrations at the bottom and top surfaces respectively, b is the film thickness, and $h = h_0/D$. The full solution of this set of equations is written out in the Appendix as an infinite series. Assuming a very thin film, I can truncate the series and obtain a first-order expression for the concentration of solute in the water film adjacent to the bottom surface:

$$c|_{y=0} = \frac{c_{sb} + c_{s0}}{2}\left(1 - e^{-\sqrt{\frac{2h}{b}}x}\right). \tag{3}$$

Equation (3) shows that near the edge of the water film ($x \approx 0$), the solute saturation is determined by the background saturation of the reservoir, which in this case is zero. Because the concentration of solute is constant at the edge of the water film, there is no flux between the top and bottom surfaces, and therefore from equation (1), the ratio of the total

material dissolved at the bottom surface to the material dissolved at the top surface is simply c_{s0}/c_{sb}. When $x >> \sqrt{b/2h}$, the solution becomes oversaturated with respect to the bottom surface, and material can only be dissolved at the top surface. The bottom surface is thus "shielded" or may even be a site of precipitation. Over time this dissolution-shielding will cause the boundary to migrate in the direction of increasing y. To estimate the length scale at which dissolution-shielding becomes appreciable, I consider measurements made by Rimstidt and Barnes (1980). They reported that for a saturated silica-water system, $h_0 = 10^{-11}\text{ms}^{-1}$. The diffusivity of the structured water in a thin film has been estimated to be four to five orders of magnitude lower than that of bulk water (Rutter, 1983), therefore $D \approx 10^{-14}\text{m}^2\text{s}^{-1}$. Assuming a water-film thickness of $1-10\text{nm}$, we can see that the length scale $\sqrt{b/2h}$ is on the order of $10^{-5}\text{m} - 10^{-6}\text{m}$. Contact lengths on this scale and larger are certainly found in rocks undergoing pressure solution. Furthermore, if we consider a more realistic scenario, where the background saturation in the reservoir is nonzero, we conclude that even smaller contacts can exhibit dissolution shielding.

The main result in this section is that a small solubility contrast may cause highly asymmetric dissolution at a pressure-solution contact. There are many implications to this result. Consider, for example, the anticrack model proposed by Fletcher and Pollard (1981). The authors create their anticrack by cutting out a thin elliptical lamina (representing the dissolved material) from an elastic medium, and then bringing the walls of the resultant crack into perfect contact along the major axis of the ellipse. The anticrack now propagates in response to the self-stress concentrations at its tips. If the lamina is symmetric, the propagation is in-plane. However, if the dissolution is asymmetric, i.e., there is more dissolution on one side of the anticrack than on the other, the removed lamina is also asymmetric. In this case, the principal stress directions at the anticrack tip are rotated relative to the anticrack plane, and the propagation direction is no longer in-plane.

DISCUSSION

In this section I continue to study the implications of the proposed dissolution-shielding effect. The chemical potential μ that drives dissolution at the interface between a solid and a free fluid can be written as (Asaro and Tiller, 1972)

$$\mu = \mu_0 - \sigma_{nn}\Omega + \frac{1}{2}\sigma_{ij}\varepsilon_{ij}\Omega + \gamma\kappa\Omega, \tag{4}$$

where μ_0 is the intrinsic chemical potential of the solid, Ω is the specific atomic volume, γ is the surface-energy density, κ is the surface curvature, σ and ε are the stresses and the strains, and n is the normal to the interface. Heidug (1995) generalized equation (4) to account for a structured water film, by including a hydration potential in the chemical potential term, and by noting that the normal stress is supported by the sum of the hydrostatic pressure and the hydration forces in the film. The second term on the right-hand side of equation (4) represents work exchanged between the solid and the fluid when mineral dissolves or precipitates, the third term is the elastic-strain-energy term, and the fourth term is a surface-energy term. Because $\varepsilon_{ij} << 1$, the work term in equation (4) is typically orders of magnitude larger than the strain energy term. For this reason, the contribution of the elastic strain energy to the overall pressure-solution rate at a pressure-solution contact is generally ignored. However, the elastic strain energy can be a very significant component of the solubility *difference* across the contact. Because the water film partially decouples non-normal tractions, the nonhydrostatic loading induces a strain-energy discontinuity across the contact. The normal traction, on the other hand, has to be continuous. Therefore, if it is assumed that both top and bottom surfaces have the same composition and that the water film separating them is very thin, their solubility difference is simply given by

$$\delta\mu = \frac{1}{2}\delta(\sigma_{xx}\varepsilon_{xx})\Omega - \gamma(\delta\kappa)\Omega. \tag{5}$$

If we assume that the water film is also very thin compared to the length scale associated with the curvature, then the surface-energy term in equation (5) can be ignored, and we are left with

$$\delta\mu \approx \frac{1}{2}\delta(\sigma_{xx}\varepsilon_{xx})\Omega \tag{6}$$

Let us now consider the contact between two different-sized elastic spheres that are composed of the same material and are pressed together in the direction of a vector connecting their centers. The elastic-strain-energy density is greater on the surface of the large sphere than on the surface of the smaller sphere. As we have seen in the previous section, even a small difference in solubility can sometimes determine the relative proportions of materials dissolved and removed on either side of a pressure solution

contact. Thus, the greater strain energy on the surface of a large sphere (or pebble or grain) can cause it to be penetrated by a sphere with a smaller radius of curvature. Another example is an undulating pressure-solution contact. If the maximum effective principal stress is much larger than the other effective principal stresses, a mineral-water interface becomes unstable to perturbations in its geometry, and an undulating contact can develop spontaneously (Gal et al., 1998). The instability is driven by the elastic strain-energy, which is relatively high at the "valleys" of the perturbation, and low at its "ridges". Consequently, one obtains domains of elastic-energy difference along the undulating contact, where a ridge with a relatively low elastic strain energy, is directly opposite a depression with a relatively high elastic strain energy. These may be the "polarized dissolution domains", anticipated by Guzzetta (1984), that facilitate stylolite growth.

The amount of material removed at a pressure-solution contact, by dissolution at the interfaces between the solid and the fluid, followed by diffusion out of the contact, is a function of the normal stress (Rutter, 1983; Lehner and Bataille, 1985). The contribution of the elastic strain energy to the total amount of material removed from the contact is negligible. However, by the dissolution-shielding mechanism I have described, the elastic strain energy can determine the proportion that each of the adjacent surfaces contributes to that total amount. This effect can cause grain-boundary migration, and facilitate the development of pitted pebbles and other pressure-solution phenomena such as stylolites. I believe that it needs to be considered in any evaluation of deformation resulting from pressure solution.

ACKNOWLEDGMENTS

This work was done in collaboration with Amos Nur, and the support came from the Basic Science Division at the Dept. of Energy, Grant # DE-FG03-86ER 13601-A010.

REFERENCES

Asaro, R.J., and Tiller, W.A., 1972, Interface morphology development during stress corrosion cracking: Part I, via surface diffusion: Met. Trans., v. 3, p. 1789-1796.

Delair, J., and Leroux, C., 1978, Methods of estimating material lost during stylolitization and the mechanisms of fracture deformation of limestones: Soc. Geol. Fr. Bull., v. 20, p. 137-144.

Fletcher, R. C., and Pollard, D. D., 1981, Anticrack model for pressure solution surfaces: Geology, v. 9, p. 419-424.

Gal, D., Nur, A., and Aharonov, E., 1998, Stability Analysis of a Pressure Solution Surface: submitted to Geophysical Research Letters.

Guzzetta, G., 1984, Kinematics of stylolite formation and physics of the pressure solution process: Tectonophysics, v. 101, p. 383-394.

Heidug, W. K., 1995, Intergranular solid-fluid phase transformations under stress: The effect of surface forces: Journal of Geophysical Research, v. 100, p. 5931-5940.

Israelachvili, J.,1991, Intermolecular and surface forces: 2nd ed., Academic Press, San Diego, California.

Lasaga, A.C., 1981, Rate laws of chemical reactions: Reviews in Mineralogy, v. 8, p. 1-68.

Lehner, F.K., and Bataille, J., 1985, Non-equilibrium thermodynamics of pressure solution: Pure Appl. Geoph., v. 122, p. 53-85.

Rimstidt, J. D., and Barnes, H. L., 1980, The kinetics of silica water reactions: Geochimica et Cosmochimica Acta, v. 44, p. 1683-1699.

Rutter, E. H., 1983, Pressure solution in nature, theory and experiment: Journal of the geological society of London, v. 140, p. 725-740.

Trurnit, P, 1968, Pressure solution phenomena in detrital rock: Sedim. Geol., v. 2, p. 89-114.

APPENDIX

FULL SOLUTION OF DIFFUSION EQUATION

The full solution to the diffusion problem defined by equation (2) is

$$c = \frac{(c_{s0} - c_{sb})hy + c_{s0}(1 - hb) + c_{sb}}{2 - hb} + \sum_{i=1}^{\infty} A_i \left(\cos(\lambda_i y) - \frac{h}{\lambda} \sin(\lambda_i y) \right) e^{-\lambda_i x},$$

where,

$$A_i = \frac{2}{\left(\lambda_i^2 + h^2\right)b + 2h} \left\{ \left[\alpha(1 + hb) + \beta h \right] \cos \lambda_i b - \left[\alpha \left(\frac{h}{\lambda_i^2} - b \right) - \beta \right] \lambda_i \sin \lambda_i b - \alpha + h\beta \right\}$$

$$\alpha = \frac{h(c_{sb} - c_{s0})}{2 - hb} \qquad \beta = -\frac{(1 - hb)c_{s0} + c_{sb}}{2 - hb} \tag{A1}$$

and λ_i are the roots of the equation

$$\tan(\lambda b) = \frac{2\lambda h}{\lambda^2 - h^2}. \tag{A2}$$

CHAPTER 4

GROWTH AND PROPAGATION OF STYLOLITES

ABSTRACT

I propose that stylolites originate as a result of an elastic strain energy discontinuity across a pressure solution interface. Assuming that the interface, which is approximately normal to the maximum principal stress, has a low shear strength, a small perturbation will become unstable and grow provided the local tangential stress it experiences is tensile. This condition occurs, for example, if the regional stress field is extremely non-hydrostatic, or at grain contacts, when the pore fluid pressure is low. Furthermore, I suggest that a single perturbation can induce other perturbations, or 'satellites', at its periphery, that grow, and in turn produce their own satellites. Thus, a perturbation does not only grow in amplitude, but it also propagates along the seam.

To explore these ideas, I conducted computer simulations of stylolite nucleation and growth. Starting with a single 'bump' at a pressure solution surface, I compute the stress using a finite element code, and use the calculated chemical potential to determine the differential dissolution at each point. The geometry of the interface is then changed accordingly, and the steps repeated. The results support the mechanism described above, and they also show that: a) the stylolite seam tapers off towards its ends, i.e. the height of individual columns decreases, b) one effect of surface energy at the pressure solution interface is to eliminate the shorter perturbation wavelengths, c) a more soluble rock can penetrate a less soluble rock, provided the radius of curvature at the contact is small enough, and d) when two adjacent rock units do not have the same stiffness, the compliant one undergoes more dissolution, and the whole seam may sag. Finally, I suggest that stylolites eventually stabilize because, as they grow, the normal stress falling on the pressure solution interface decreases, until presumably, other 'flatter' pressure solution seams are activated and take up the strain.

INTRODUCTION

Stylolites are geometrically irregular pressure solution interfaces in rock, where both sides exhibit mutual interpenetration. They may appear as micro-stylolites at grain contacts, or form stylolite seams that can propagate through rock for tens of meters or more

(Bushinskiy, 1961; Dunnington, 1967). The individual indentations generally point in the direction of maximum compressive stress, which usually (but not always) is approximately normal to the seam (Stockdale, 1922; Heald, 1955). Pressure solution at stylolite seams may result in strains as large as 50% that can, in places, greatly exceed crustal deformation achieved by other means, such as folding and faulting (Alvarez et al., 1978).

Many rock types contain stylolites (Park and Schot, 1968), but it is in limestones and sandstones where they are the most common and striking. In these rocks, stylolites can have a tremendous impact on reservoir structure and fluid transport. The seams are usually marked by an insoluble residue that often forms a permeability barrier. Also, the vast amount of cement, produced by dissolution at pressure solution seams, causes porosity loss and compartmentalization in the host reservoirs. Stylolites are indicative of the history of their geological setting: Trurnit (1968) has pointed out that the large vertical strains associated with stylolite formation, must have caused pore fluid migration on scales up to that of whole tectonic basins. Stylolite columns are frequently used to infer the direction of the maximum compressive stress, and for this reason, they are also frequently associated with, and roughly perpendicular to, tension gashes (Bushinskiy, 1961; Elliot, 1973; Rispoli, 1981; Fletcher and Pollard, 1981). Later, I will discuss this point further, in view of the findings reported here.

Understanding how stylolites form, and why they evolve the unique geometries we see, has long been a major challenge, as well as an issue of controversy. Some of the most important ideas were put forward by Stockdale (1922), who recognized stylolites in Indiana limestone as post-lithification pressure solution phenomena, Fletcher and Pollard (1981) who showed that the stress and strain fields associated with stylolites, and their manner of propagation, can be explained by modeling them as anticracks, and Dewers and Ortoleva (1990), who used reaction/transport and mechanical modeling to explore conditions that would favor localized versus pervasive pressure solution. However, no one has yet successfully explained some of the most difficult questions that are raised by the occurrence of stylolites: how can one reconcile their strikingly irregular geometry with our knowledge of pressure solution physics? How do they form, and do they stabilize? In this chapter, I attempt to answer some of these questions.

I suggest that stylolite growth is driven by elastic strain energy differences in rock on either side of boundary layer that has a low shear strength. This boundary layer may be a water film as proposed by Weyl (1959), a clay parting holding adsorbed water (Rutter, 1983), or a channel-island type boundary structure (Raj, 1982). I show that when the maximum principal stress is normal to the boundary layer, a small perturbation at the interface can grow, provided that the stress normal to the boundary is very high compared

to the lateral stress. Furthermore, it is demonstrated that this perturbation can induce the formation of 'satellite' perturbations adjacent to itself, and so propagate laterally as well as increase in amplitude. I use computer-assisted simulation to study some representative cases.

STYLOLITES: NUCLEATION AND PROPAGATION

In Chapter 2, I have shown that a mineral surface, undergoing pressure solution, can become morphologically unstable under certain stress conditions. This instability is driven by variations in the elastic strain energy, causing one part of the surface to become more soluble than another. Let us now consider a pressure solution interface, and model its elastic properties as those of a low shear-strength (high Poisson ratio) linear-elastic layer separating two mineral surfaces. I introduce a small profile fluctuation in the boundary layer, by having a small 'bump' in one material project into a depression in the other. If I now apply uniaxial loading perpendicular to the layers, the mineral layers undergo lateral Poisson dilation. The boundary material, however, cannot support a large shear stress, and so its stress state is close to hydrostatic -- and equal in magnitude to the uniaxial load. As a result the bump is compressed by the boundary material, while the depression is dilated. Because these fluctuations are superposed on the generally extensional state of strain, we find that the bump has a smaller net elastic energy, and so is less soluble, than the depression it fits into. Under these conditions, the perturbation can grow, provided, that the resultant change in surface energy, is no greater than the elastic energy difference driving this growth. Notice also, that the elastic strain energy in the mineral above the boundary layer, and adjacent to the bump, is lower than the one in the mineral directly below (Figure 1a). This strain energy discontinuity will enable differential dissolution across the interface, and consequently two 'satellites' will form, one on each side of the bump, growing in the opposite sense to the parent bump. This process will repeat, satellites growing and inducing their own satellites, and in this way, the perturbation not only grows in amplitude over time, but it also propagates along the seam. Figure 1b shows the strain energy field after two pairs of satellites have began to grow.

Let us now apply compressive stress at the horizontal boundaries, but still maintain the vertical stress as the maximum principal stress. Compressive stresses will concentrate near the top of the perturbation, and will counter-act the tensile stresses and strains that were driving its growth. The net result is to lower the elastic strain energy above the perturbation and increase it below. At a critical ratio of horizontal to vertical boundary loads, the perturbation amplitude begins to decay (see Chapter 2)

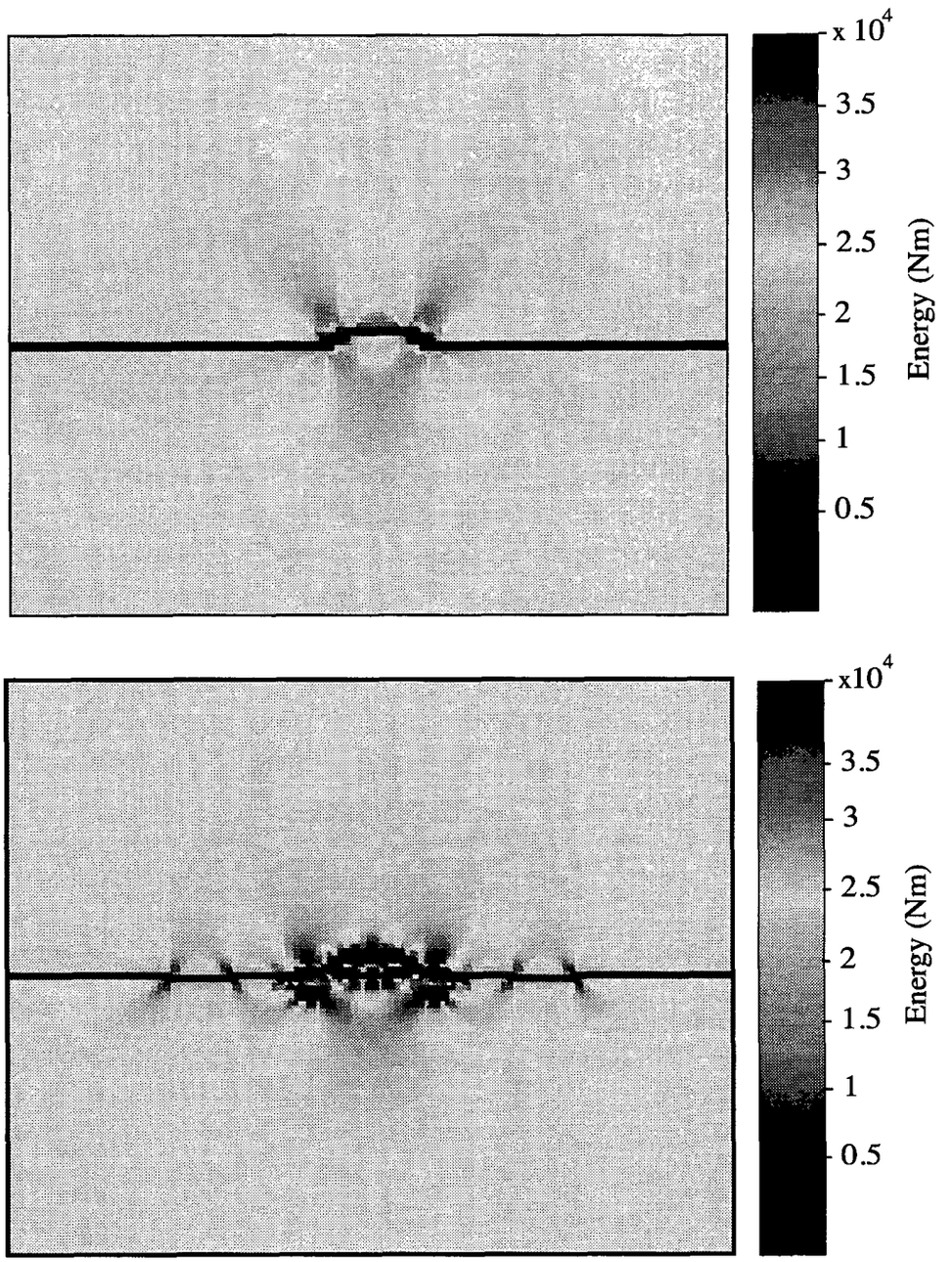

Figure 1: The elastic strain energy in the initial configuration (a), and after two time steps (b). Note the oscillatory pattern of strain energy contrasts.

COMPUTATIONAL METHOD AND ASSUMPTIONS

To examine the ideas outlined above, I ran computer simulations of stylolite nucleation and growth. I begin with a two-dimensional linear-elastic system, consisting of two thick parallel layers, that have the same elastic moduli, and are separated by a low shear-strength thin layer. A small perturbation is introduced into this thin boundary, by letting a bump from the bottom layer, project into a depression in the top layer, while maintaining the boundary between them continuous. The stress field is then computed using a finite element code, and I calculate the chemical potential on either side of the boundary using the equation (Asaro and Tiller, 1972)

$$\mu(s) = \mu_0 + \Omega\left(\gamma\kappa(s) + u_e - \sigma_{nn}\right). \tag{1}$$

Here s is the coordinate along the solid/fluid interface, μ_0 is the intrinsic chemical potential of the unstrained material, Ω is the atomic volume, γ is the interfacial energy density, κ the curvature of the surface, u_e the elastic strain energy, and σ_{nn} the stress normal to the boundary. For stress regimes that allow the formation of pressure solution contacts, this last term dominates the right-hand side of Equation (1), and therefore determines, together with a transport factor, the total flux of material out of the contact (Lehner and Bataille, 1985). Next, at each point along the boundary where σ_{nn}, and therefore $\mu(s)$, exceed an assumed threshold, material is removed. The total amount of material removed at these points is directly proportional to the local value of σ_{nn}. To determine the amount each one of the two adjacent surfaces contributes to this total, I consider their solubility difference. If σ_{nn} remains constant across the boundary, the chemical potential difference between the two surfaces is

$$\delta\mu(s) = \delta\mu_0 + \Omega\left(\gamma\delta\kappa(s) + \delta u_e\right). \tag{2}$$

We saw, in Chapter 3, that this small solubility difference, can have a profound impact on the dissolution, at a thin pressure solution contact. Although it has a negligible effect on the total flux out of the contact, it can severely inhibit the dissolution of the less soluble surface. In this model, the boundary is assumed to be thin enough, initially, so that only the more-soluble surface dissolves, while the less-soluble one remains intact. As the geometry evolves, the boundary may become locally thicker because of geometrical miss-

matching. I assume that at these thicker parts of the boundary, $\delta\mu(s)$ can no longer couple the two surfaces efficiently, and therefore equal amounts dissolve on each side. Note that because the profile of each surface has changed, they may no longer match each other, and some spaces can exist between them. These spaces tend to disappear after a few iterations, because the normal stress there is lower than it is on other parts of the pressure solution contact. The high normal stress sections will dissolve faster, and thus wipe out the spaces.

RESULTS

In this section I report the results of several simulation runs, and examine the effect of varying some of the controlling parameters in the system. In all runs, the maximum compressive stress is normal to the initially flat, pre-existing, boundary layer. The Appendix contains a more detailed record of the simulation results.

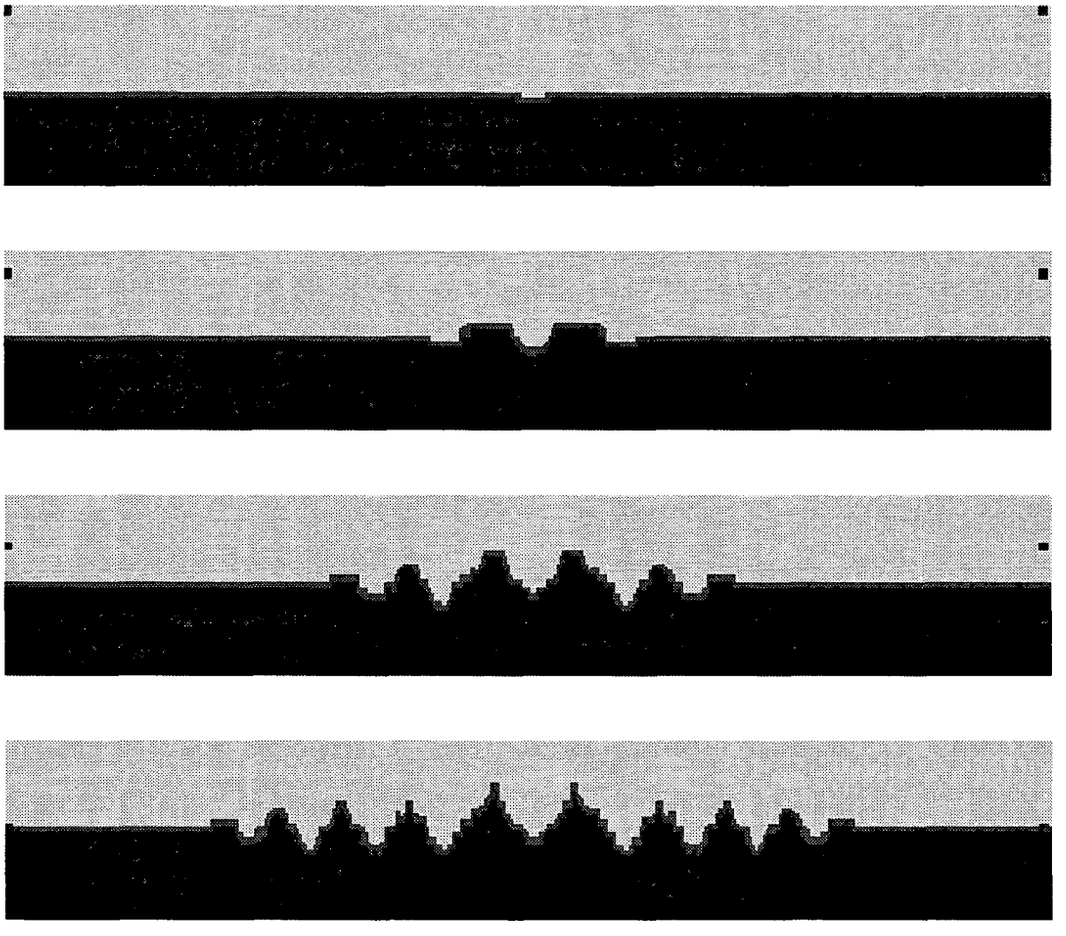

Figure 2: Evolution of a stylolite seam: the stylolite grows in amplitude and spreads laterally until it stabilizes. Tapering of stylolite seams has often been observed in the field.

General

In Figure 2, I show the evolving geometry of the model during a typical run. There is a zero-effective-stress boundary condition on a vertical line bisecting the stylolite, representing a vein, and a zero-lateral-displacement boundary condition at the left and right edges. It is easy to observe the growth and propagation of the initial perturbation, in a manner consistent with the ideas I have discussed previously. The perturbation grows in height as expected, and it induces the formation of 'satellites' adjacent to it. This process repeats, and the seam takes on a tapered appearance. Tapering of a stylolite at its ends is indeed a commonly made field observation (Stockdale, 1922; Bushinskiy, 1961; Trurnit, 1968). Eventually, growth is arrested, and the stylolite stabilizes. When the zero-stress boundary condition was removed, the stylolites decayed as expected.

Effect of Surface Energy

Introducing a finite surface energy into the simulation, resulted in a larger dominant wavelength (Figure 3). This happens because the ratio of surface area to volume is larger for the shorter wavelengths, and therefore in order to overcome the surface energy, they generally requires a higher strain energy density than does a wider, longer wavelength perturbation. For a more quantitative treatment of this issue, see Chapter 2. If the perturbation wavelength is large relative to the boundary thickness, the dissolution is more asymmetric than if it is small (Chapter 3). Therefore, the simulation with the surface energy produced a larger, better formed stylolite.

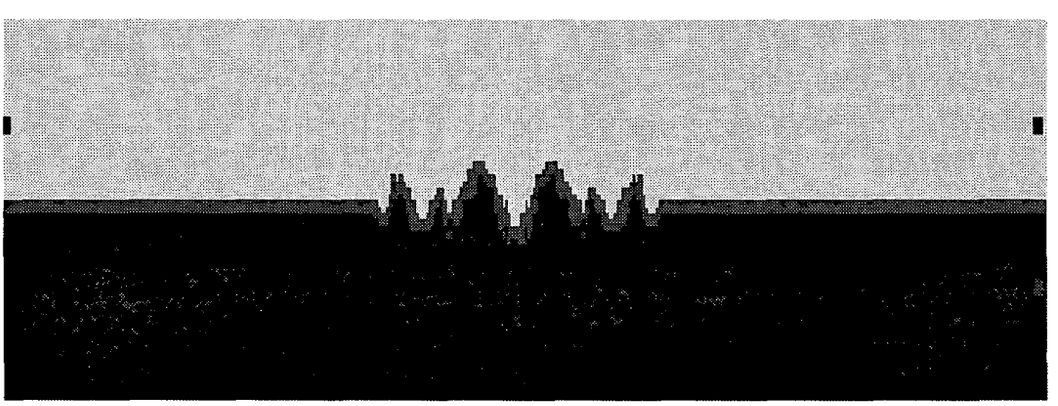

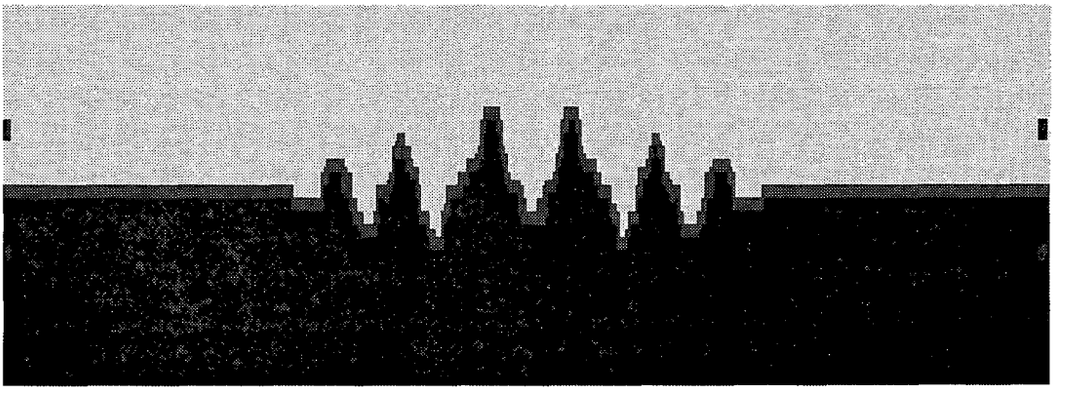

Figure 3: Perturbation growth after three time steps a) without surface energy, b) with surface energy. Note elimination of shortest wavelengths

Effect of Solubility Difference

A difference in intrinsic solubility of the two layers, does not necessarily mean that the more soluble rock will always undergo greater dissolution. This may be true in the average sense, but locally, if a portion of the surface of the more soluble rock has a small radius of curvature, the induced elastic strain energy difference may be sufficient to offset the intrinsic solubility difference. Thus narrow projections of the more soluble rock may penetrate into the less soluble rock (Figure 4). There are many examples of this phenomenon, one of the most common of which, are examples of small pebbles penetrating larger ones, despite being intrinsically more soluble (Stockdale, 1922; Bushinskiy, 1961).

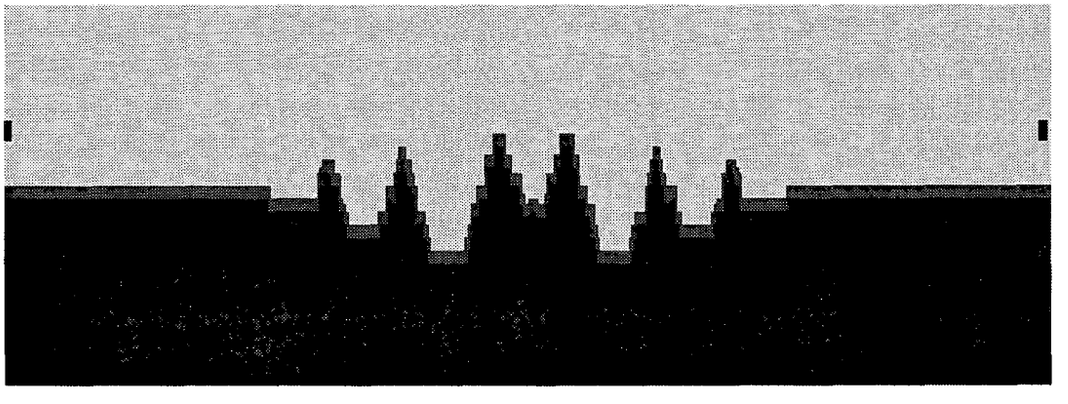

Figure 4: The less soluble material (top) is penetrated by thin projections of a more soluble rock (bottom).

Effect of Elastic Moduli Difference

If one material is more compliant, it will store more elastic strain energy, that (barring other property differences) will make it more soluble than the stiffer layer. The elastic energy difference is greatest away from the vertical free boundary bisecting the stylolite. As a result a 'sag' may develop in the seam (Figure 5). Examples of sagging stylolite seams are given by Stockdale (1922).

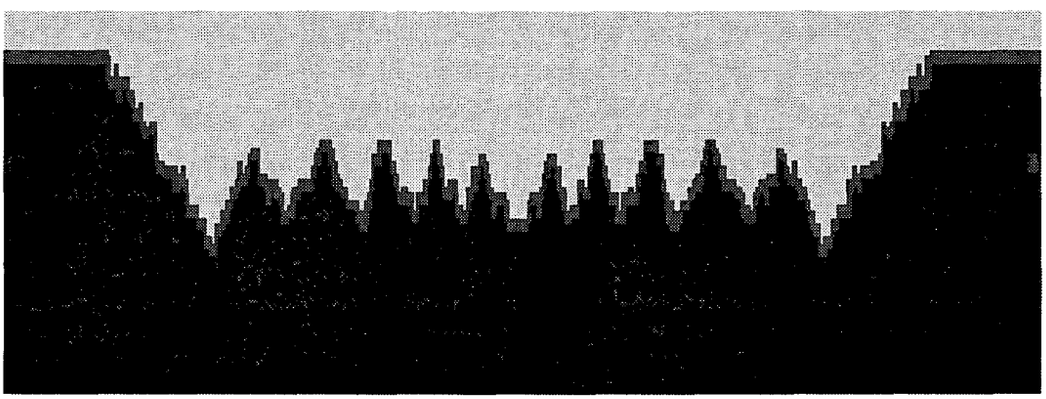

Figure 5: The top layer is softer, and stores more elastic strain energy than the bottom layer. The difference in energies is especially great away from the free boundary, and the result is a sagging stylolite seam.

CONCLUSIONS

I propose that stylolite growth is driven by a discontinuity in the elastic strain energy across the pressure solution interface. If the maximum compressive stress is normal to the interface, as is often the case in pressure solution seams and grain contacts, a small perturbation destabilizes and grows, provided the stresses at its tip are tensile. Thus, I believe that development of stylolites is indicative of a very low minimum principal stress, or in the case of grain contacts, a low pore fluid pressure. Moreover, I suggest that a single perturbation can induce other perturbations, or 'satellites', at its periphery, that in turn produce more satellites, and so on. Thus a single heterogeneity can induce the stylolitization of the whole pressure solution seam, since it grows both in amplitude and it propagates along the seam. To test this idea, I have conducted computer-assisted simulations of stylolite nucleation and growth. The results support the nucleation and growth mechanism I have suggested, and they also seem to replicate often observed features, such as tapering and sagging in stylolite seams.

I suggest that stylolites eventually stabilize because, as the stylolite seam grows, some parts of the evolving interface are not favorably oriented to participate in pressure solution (e.g., the sides of the stylolites), however they do take on some of the normal stress burden. Consequently, the normal stress on the pressure solution interface drops, and other, 'flatter', pressure solution seams are activated nearby to take up the strain.

ACKNOWLEDGMENTS

Amos Nur collaborated with me on this work, and it was supported by the SRB.

REFERENCES

Alvarez, W., Englender, T., and Geiser, P.E., 1978, Classification of solution cleavage in pelagic limestones: Geology, **6**, 263-266.

Asaro, R.J., and Tiller, W.A., 1972, Interface morphology development during stress corrosion cracking: Part I, via surface diffusion: Met. Trans., **3**, 1789-1796.

Bushinskiy, G.I., 1961, Stylolites: Jzv. Akad. Nauk. S.S.S.R., Ser. Geol., **8**, 31-46.

Dewers, T., and Ortoleva, P., 1990, A coupled reaction/transport/mechanical model for intergranular pressure solution, stylolites, and differential compaction and cementation in clean sandstones: Geochim. and Cosmochim. Acta, **54**, 1609-1625.

Dunnington, H.V., 1967, Aspects of diagenesis and shape change in stylolitic limestone reservoirs: Seventh World Petroleum Congress Proceedings (Mexico), **2**, 339-352.

Elliot, D., 1973, Diffusion flow laws in metamorphic rocks: GSA Bulletin, **84**, 2645-2664.

Fletcher, R.C. and Pollard, D.D., 1981, Anticrack model for pressure solution surfaces: Geology, **9**, 419-424.

Heald, M.T., 1955, Stylolites in Sandstones: J. Geol., **63**, 101-104.

Lehner, F.K., and Bataille, J., 1985, Non-equilibrium thermodynamics of pressure solution: Pure Appl. Geoph., **122**, 53-85.

Park, W.C., and Schot, E.H., 1968, Stylolites: their nature and origin: J. Sedim. Petrol., **38**, 175-191.

Raj, R., 1982, Creep in polycrystalline aggregates by matter transport through a liquid phase: Journal of Geophysical Research, **87**, 4731-4739.

Rutter, E.H., 1983, Pressure solution in nature, theory, and experiment: Geological Society of London Journal, **140**, 725-740.

Rispoli, R., 1981, Brittle kink-bands and stress variations in the jurrasic limestones of the Languedoc (southern France): Tectonophysics, **75**, T29-T36.

Stockdale, P.B., 1922, Stylolites: their nature and origin: Indiana Univ. Studies, **9**, 1-97.

Trurnit, P, 1968, Pressure solution phenomena in detrital rock: Sedim. Geol., **2**, 89-114.

Weyl, P.K., 1959, Pressure-solution and the force of crystallization -- a phenomenological theory: Journal of Geophysical Research, **64**, 2001-2025.

CHAPTER 5

A PHYSICAL MODEL FOR POROSITY REDUCTION IN SANDSTONES

ABSTRACT

The experimental elastic moduli-porosity trends for clean sandstones can be described by the modified upper Hashin-Shtrikman (MUHS) bound. One geometrical (but not necessarily geological) realization is: as porosity decreases, the number of the pores stays the same and each pore shrinks while maintaining its shape. This concept of uniform porosity reduction implies that permeability is proportional to the effective porosity squared, and that formation factor is proportional to the inverse of the effective porosity. The effective porosity here refers to the part of the pore-space that dominates fluid flow. The proposed relations for permeability and formation factor agree well with the experimentally observed values. These laws are different from the often used forms of the Kozeny-Carman equation and Archie's law, where permeability is proportional to the total porosity cubed and formation factor is proportional to the inverse of the total porosity squared, respectively. I suggest that the uniform porosity reduction concept be used in consolidated rocks with porosities below 0.3. The transition from high-porosity unconsolidated sands to consolidated sandstones can be described by the cementation theory: the MUHS moduli-porosity curves connect with those predicted by the cementation theory at the porosity of about 0.3. This scheme is not appropriate for modeling other porosity reduction mechanisms such as glass bead sintering, because during sintering, the pores do not maintain their shapes, rather they gradually evolve to rounder, stiffer pores.

INTRODUCTION

An outstanding rock physics problem is the use of acoustic methods to estimate permeability in situ. One approach to this problem is by understanding the internal structure of rock. Indeed, at the same porosity, different rock samples may have completely different pore shapes. Resulting from this variability are permeability and velocity scatters, often observed experimentally. Both acoustic velocity and permeability are affected strongly by the structure of the pore-space in the rock. This provides a clear incentive to explore the relations between acoustic velocities and permeability through the pore-space geometry.

When a suite of data points is studied, there is always an attempt to generalize this experimental knowledge by deriving a functional dependence. Two principal approaches serve this purpose: (a) statistical correlation, and (b) theoretical modeling. In the former case, the result is a best-fit curve that is certainly usable for interpolation but lacks generality. In the second case, an idealized system is constructed whose parameters match those experimentally observed. One example of theoretical modeling is the class of self-consistent models (e.g., Zimmerman, 1991), where rock is presented as a composite with, e.g., elliptical inclusions. Usually one attempts to specify a spectrum of the void aspect ratios that will fit the experimental observation best. As a result, an experimentally observed trend is described analytically, rather than statistically. Such analytical description, if intended to be the final product of modeling, is no more useful than the statistical description. Still, there is an important advantage that theoretical modeling has over statistical correlation.

Let us assume that if, for example, the elastic moduli of a suite of samples can be matched by those of an idealized composite, then the pore-space geometry of real rocks may correspond to that of the composite. This axiom allows us to go beyond analytically matching experimental trends -- now we can use the inferred geometry to make estimates of, e.g., permeability. In this chapter I try this proposed use of theoretical modeling on a group of clean sandstones at high effective pressure. I find that an experimental elastic moduli-porosity trend can be well matched by a modified upper Hashin-Shtrikman (MUHS) bound. The corresponding idealized composite is a porous solid with an elastic quartz frame. One realization of the MUHS trend is that as porosity decreases, the number of pores stays the same, and each pore shrinks while maintaining its shape (Figure 1). The relative volume reduction is the same for all pores. It is important to emphasize, that this uniform porosity reduction scheme may not correspond to a realistic diagenetic process. I employ this idealization as a modeling tool, that is useful only as long as it produces experimentally supported results. By using this uniform porosity reduction scheme, I will show, later in the chapter, that permeability is proportional to the effective porosity squared, where effective porosity refers to the part of the pore space that dominates fluid flow. If two clean sandstone samples have effective porosities ϕ_{e1} and ϕ_{e2}, and permeabilities k_1 and k_2, respectively, then $k_1 / k_2 = (\phi_{e1} / \phi_{e2})^2$. This formula is different from the often-used form of the Kozeny-Carman equation where permeability is proportional to the total porosity cubed. The proposed porosity-permeability transformation matches experimental data in Fontainebleau sandstone very well in the entire

porosity range. The traditional Kozeny-Carman formula matches the Fontainebleau data only at high porosity.

It also follows from the proposed porosity reduction scheme that the formation factor is proportional to the inverse of the effective porosity. For two clean sandstone samples of effective porosities ϕ_{e0} and ϕ_{e1}, and formation factors F_0 and F_1, respectively, $F_0 / F_1 = \phi_{e1} / \phi_{e0}$. This formula is different from the often-used form of Archie's law, where the formation factor in clean sandstones is proportional to the inverse of the total porosity squared, and it provides a better match to the Fontainebleau data.

ELASTIC MODELS AND PORE-SPACE TOPOLOGY

Clean sandstones at high effective pressure have a distinct modulus-porosity trend. Nur et al. (1991) show that this trend is approximately an arithmetic mean of the two end members: the pure-mineral modulus at zero porosity, and zero modulus at critical porosity:

$$M = M_q(1 - \phi / \phi_c), \tag{1}$$

where M is an elastic modulus of a sandstone, M_q is the appropriate modulus for quartz, ϕ is porosity, and ϕ_c is the critical porosity. The latter is the porosity above which sand can exist only as a suspension. The ϕ_c value is about 0.4, which is close to the porosity of a random pack of identical spheres -- 0.36. Mukerji et al. (1995) incorporated the critical porosity concept in the differential effective medium theory by taking the material at the critical porosity as one of the constituents of a two-phase composite.

Equation (1) -- the modified Voigt bound -- represents the stiffest possible arrangement of the two end members: pure quartz and unconsolidated sand. The physical realization of this model is an elastically anisotropic arrangement of alternating columns of sand and quartz. One can define an isotropic stiff arrangement of these end members by using the upper Hashin-Shtrikman bound that is rescaled from the porosity interval between 0 and 1 to the interval between 0 and ϕ_c (Chen, 1992). A physical realization of this bound is a Hashin type assemblage of spheres of different sizes that fill the whole space (Hashin, 1962). Each sphere consists of a smaller sand sphere embedded in a quartz shell. Although the elastic moduli, as given by the two models, fit the experimental data well, the inferred rock structure is unrealistic and thus cannot be used for estimating the transport properties of the rock. My goal is to find a physical realization of the modified upper

Hashin-Shtrikman bound such that the inferred permeability and formation factor are consistent with experimental measurements.

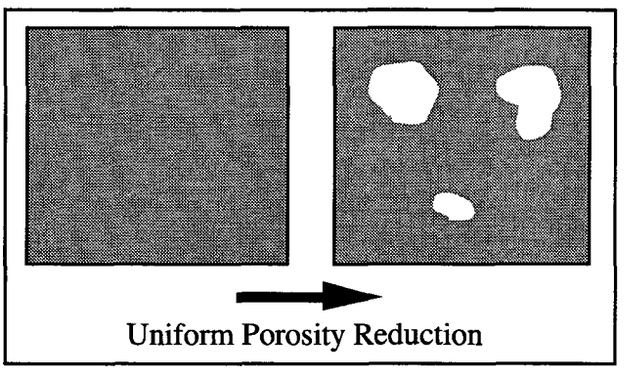

Figure 1. The porosity reduction scheme corresponding to the MUHS model.

MODIFIED UPPER HASHIN-SHTRIKMAN BOUND

To model the elasticity of dry sandstone, let us examine a Hashin type (Hashin, 1962) assemblage of different-sized quartz spheres, ranging down to infinitesimal size, that fills the whole space. Each quartz sphere contains a randomly oriented non-spherical pore centered at its origin. All spheres have the same porosity, ϕ_0, which is the porosity of the sandstone, and all pores have the same shape. Because of the statistical uniformity of this assemblage and the random orientation of the spheres, we can assign to each sphere an effective bulk modulus K_0. Consequently, this is the bulk modulus of the entire assemblage.

Let us assume that the assemblage is subject to hydrostatic loading, and consider a single sphere in the assemblage. By regarding the remainder of the assemblage as an effective medium, the loading on the sphere can be assumed hydrostatic. I reduce the porosity of the sphere from ϕ_0 to ϕ by letting the pore inside it shrink uniformly. The shape of the pore stays the same, therefore the new sphere (with porosity ϕ and bulk modulus K) is simply a downsized version of the original sphere (with porosity ϕ_0 and bulk modulus K_0) embedded in a spherical quartz shell (Figure 2). The volumetric fraction occupied by the original sphere (the soft end member) is ϕ/ϕ_0, and that occupied by quartz mineral (the stiff end member) is $1-\phi/\phi_0$. By repeating this process for every sphere in the assemblage, I obtain the physical realization of the upper Hashin-Shtrikman bound for the bulk modulus: spheres of the softer end member (the original sandstone)

embedded in spheres of the stiff end member (quartz mineral). The bulk modulus of each composite sphere, and thus of the assemblage is

$$K = K_q + \frac{\phi/\phi_0}{\dfrac{1}{K_0 - K_q} + \dfrac{1-\phi/\phi_0}{K_q + \dfrac{4}{3}\mu_q}}, \tag{2}$$

where K_q and μ_q are the quartz bulk and shear moduli, respectively. The modified upper Hashin-Shtrikman bound (with these end members) for the shear modulus is:

$$\mu = \mu_q + \frac{\phi/\phi_0}{\dfrac{1}{\mu_0 - \mu_q} + \dfrac{2(1-\phi/\phi_0)(K_q + 2\mu_q)}{5\mu_q(K_q + \dfrac{4}{3}\mu_q)}}. \tag{3}$$

Formulas (2) and (3) are the original Hashin-Shtrikman upper-bound formulas scaled from the $[0,1]$ porosity interval to the $[0,\phi_0]$ interval. The theoretical curves predicted by these formulas are compared to the bulk and shear moduli measured by Han (1986) on a set of clean sandstones (Figure 3). In this example, the high-porosity end member chosen was the highest porosity sandstone in the set with $\phi_0 = 0.22$, $K_0 = 16.4$ GPa, and $\mu_0 = 15.7$ GPa.

Clearly, the end member may be a different sample with porosity smaller than 0.22. Thus equations (2) and (3) can be used to extrapolate the moduli-porosity trend to higher (than the end member) porosities. These equations predict non-zero elastic moduli at porosities higher than the critical porosity. The physical reason is that a consolidated-rock model is not appropriate to describe unconsolidated granular sandstones near critical porosity. The transition from the unconsolidated state to the consolidated state can be described by the cementation theory (Dvorkin et al., 1994; Dvorkin and Nur, 1995). The MUHS curves connect with the moduli-porosity curves predicted by the cementation theory at porosity of about 0.3 (Figure 4). I conclude that the MUHS model can be used to describe consolidated sandstone (porosities up to 0.3), and the cementation theory is appropriate to describe high-porosity cemented unconsolidated sandstones.

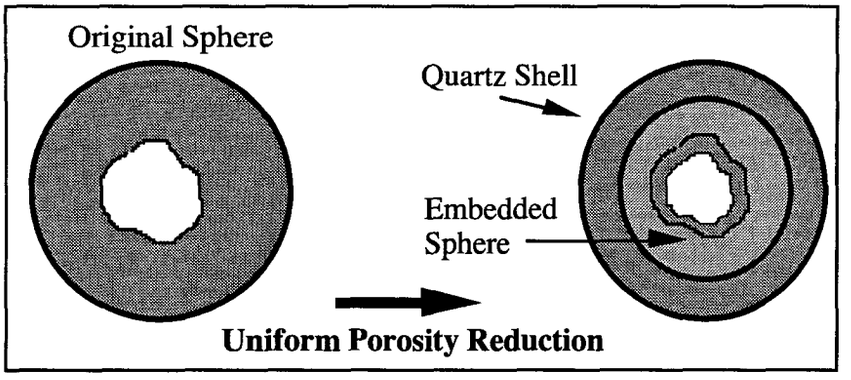

Figure 2. Shrinking pore inside a quartz sphere.

The main result of this part is that the uniform porosity reduction concept allows one to accurately predict the velocity-porosity relation in clean sandstones. To implement this concept, I used a simplified representation of rock, where individual pores are isolated. Next the same concept will be used to calculate permeability and formation factor. However, in this case I examine cylindrical tubes instead of spheres to ensure fluid and electric transport. This is another realization of the same concept that does not necessarily have to be consistent with the first realization.

In the Appendix I show that for sintered glass beads, the moduli-porosity trend does not follow the MUHS curve. This happens because, during sintering, the pores evolve to rounder, stiffer shapes.

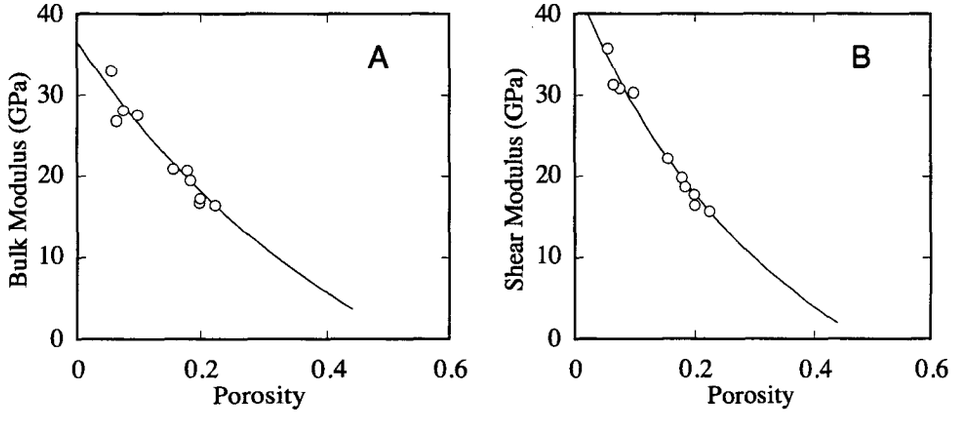

Figure 3. Dry-rock elastic moduli for clean sandstone. Solid lines are predicted by the modified upper Hashin-Shtrikman model. a. Bulk modulus. b. Shear modulus.

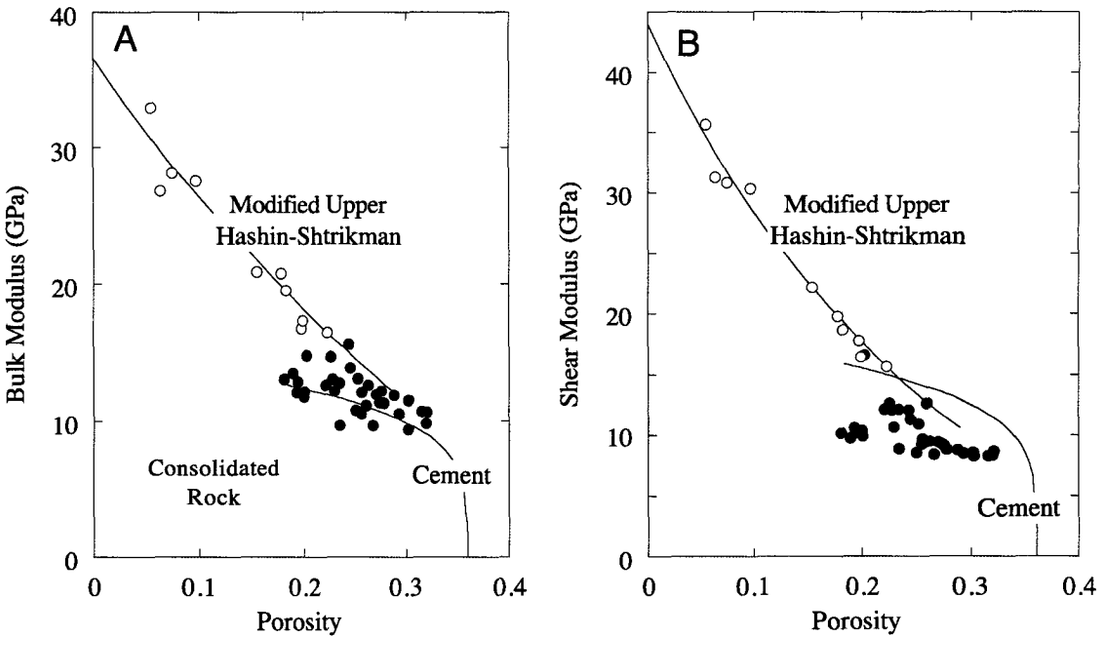

Figure 4. Model predictions for consolidated and unconsolidated sandstones. The cementation theory lines are for the case where spherical grains are uniformly coated by diagenetic quartz cement. Open circles are the consolidated clean sandstone data. Filled circles are high-porosity cemented sands from the Oseberg field (Strandenes, 1991).

PERMEABILITY MODEL AND DATA

Consider the experimental results for Fontainebleau sandstone (Bourbie and Zinsner, 1985). The authors measure the "trapped" porosity, which is the part of the pore space from where a non-wetting fluid (air) cannot be displaced by a wetting fluid (toluene) during imbibition by capillary rise and subsequent soaking. I assume that the trapped porosity is poorly connected to the conductive part of the pore-space, through narrow throats, and probably does not contribute significantly to fluid flow. Therefore, the bulk of fluid flow takes place through the complement of the trapped porosity : the free porosity. Figure 5 is a plot of the free versus total porosity in Fontainebleau sandstone (Bourbie and Zinsner, 1985). The data can be approximated by the function

$$\phi_e = 1.3486(\phi - 0.021)^{1.4}. \tag{4}$$

Now let us consider a two-dimensional cross-section of rock, and assume that fluid flow takes place in an identical set of straight uniform tubes that are perpendicular to this

plane. These tubes represent the free porosity, which I shall from now on term the "effective porosity". The permeability is then proportional to the effective porosity squared (Gueguen and Dienes, 1989) and, therefore, uniform porosity reduction means that

$$\frac{k_1}{k_0} = \left(\frac{\phi_{e1}}{\phi_{e0}}\right)^2, \tag{5}$$

where k_0, k_1 are the permeabilities of two samples, and ϕ_{e0}, ϕ_{e1} are the corresponding effective porosities. The traditional formula that follows from the Kozeny-Carman equation (with the total porosity) for constant grain size and tortuosity is

$$\frac{k_1}{k_0} = \left(\frac{\phi_1}{\phi_0}\right)^3. \tag{6}$$

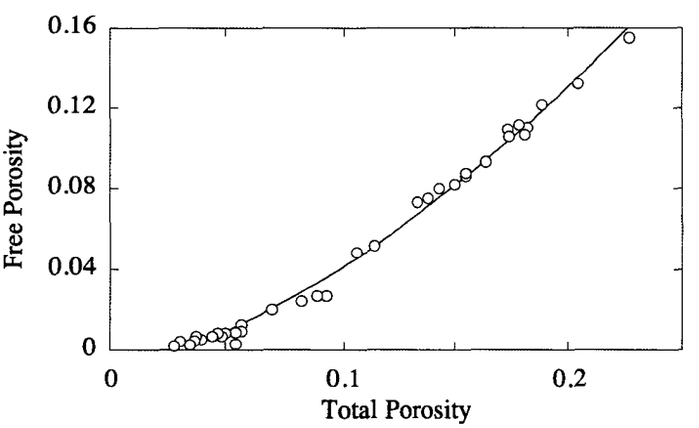

Figure 5. Free porosity versus total porosity in Fontainebleau sandstone (after Bourbie and Zinszner, 1985). Data points and the empirical fit.

To implement formulas (5) and (6) I choose the highest-porosity Fontainebleau sample (porosity ϕ_0 and permeability k_0) and calculate permeability versus porosity. If total porosity values are used in both formulas (Figure 6a), then only formula (6) matches the data (but not at small porosities). However if the effective porosity is used (Figure 6b), then formula (5), which results from the proposed porosity reduction model, approximates the data well for all porosities.

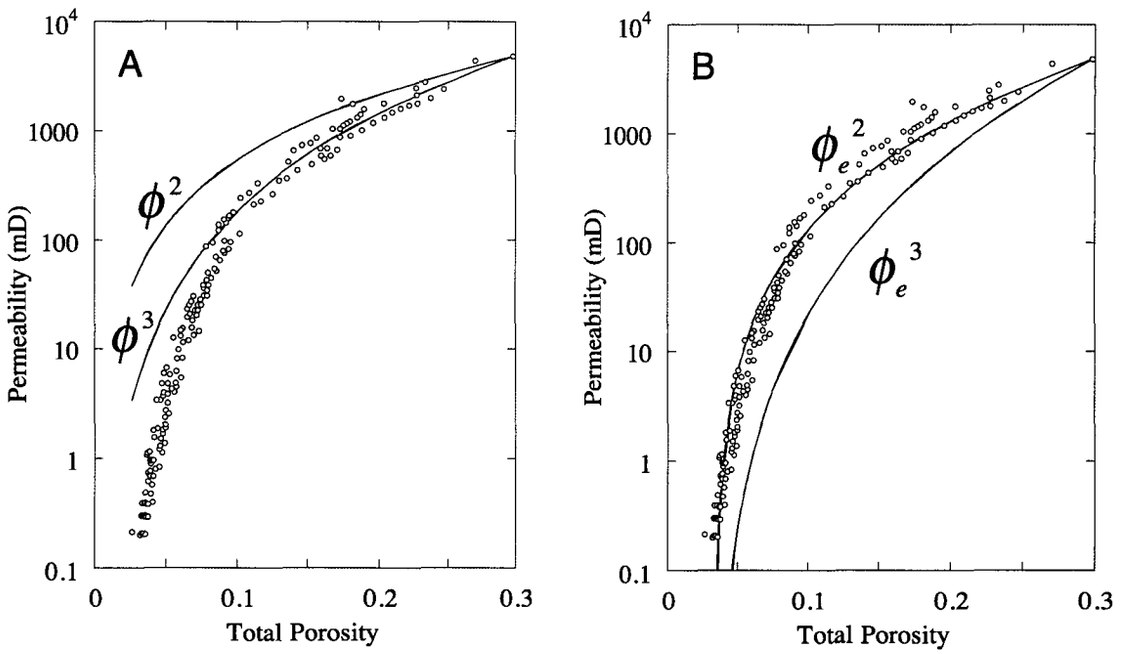

Figure 6. Permeability versus porosity: data points and theoretical predictions from formulas (4) and (5). a. Using total porosity values. b. Using effective porosity values.

FORMATION FACTOR

Let us assume that electrical transport is also dominated by the effective porosity. Then by using the same transport model as in the previous section and letting the tubes shrink uniformly, I obtain a linear relationship between the inverse of the formation factor and the effective porosity (Gueguen and Dienes, 1989):

$$\frac{F_0}{F_1} = \frac{\phi_{e0}}{\phi_{e1}}, \tag{7}$$

where F_0, F_1 are the formation factors of two rock samples, and ϕ_{e0}, ϕ_{e1} are the corresponding effective porosities. An often used form of Archie's law for clean sandstones is (Gueguen and Palciauskas, 1994)

$$\frac{F_0}{F_1} = \left(\frac{\phi_1}{\phi_0}\right)^2. \tag{8}$$

In Figure 7, I compare the formation factor data for Fontainebleau sandstone (Jacquin, 1964) with theoretical curves from formulas (7) and (8) calculated using total porosity. To implement these formulas, I choose the highest-porosity Fontainebleau sample (porosity ϕ_0 and formation factor F_0) and calculate formation factor F_1 versus porosity ϕ_1. The effective porosity is calculated from the total porosity, using equation (4) .

If the total porosity is used, Formulas (7) and (8) give, respectively, lower and upper bounds for the data. However, neither one provides a reasonable estimate. On the other hand, if the effective porosity is used, formula (7), which results from the proposed porosity reduction model, matches the data well, whereas formula (8) strongly overestimates the data.

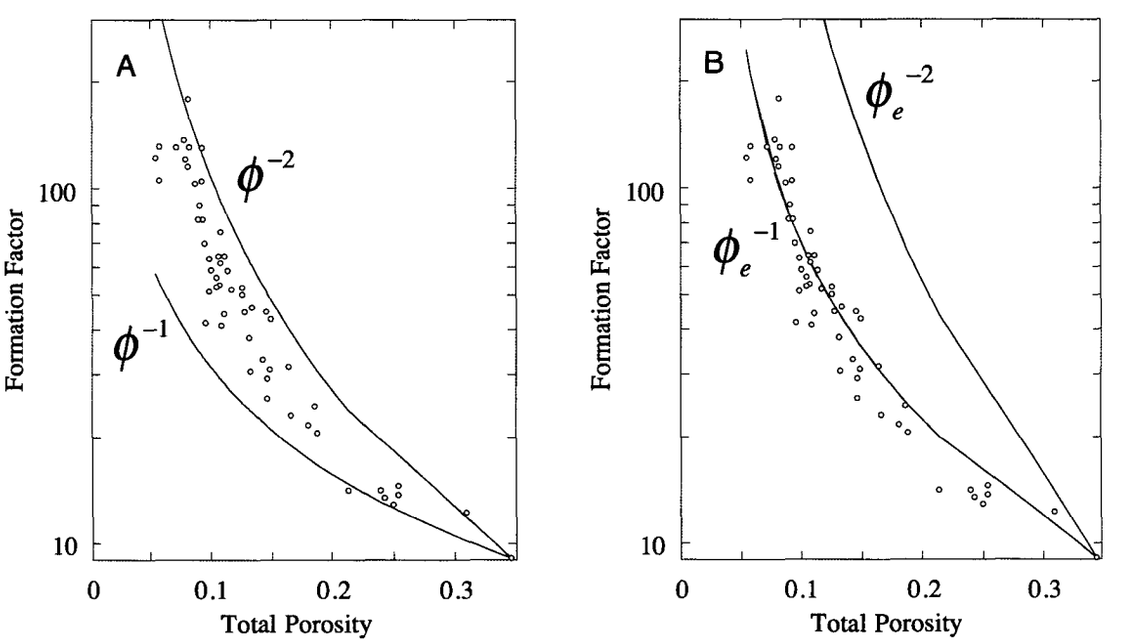

Figure 7. Formation factor versus porosity: data points and theoretical predictions, as given by formulas (7) and (8). a. Using total porosity. b. Using effective porosity.

CONCLUSIONS

Modulus-porosity trends in clean sandstones can be well matched by a modified upper Hashin-Shtrikman bound, where the zero-porosity end member is quartz mineral and the high-porosity end member is a consolidated sandstone. A porosity reduction model for sandstones that is consistent with this observation is: as porosity decreases, the number of the pores stays the same, and each pore shrinks while maintaining its shape; the relative volume reduction is the same for all pores. At a porosity of about 0.3, the MUHS modulus-porosity curve naturally connects with the moduli-porosity curves predicted by the cementation theory for uniformly coated grains. The MUHS model can be used to describe consolidated sandstone, whereas the cementation theory can be used to describe unconsolidated high-porosity cemented sandstone. Based on the uniform porosity reduction concept used in the MUHS model, I can relate porosity change to geometry change in the sandstone. This geometry, in turn, leads us to estimating permeability and formation factor from porosity in clean sandstones. Permeability is predicted to be proportional to the porosity squared, and formation factor to the inverse of porosity. These relations are different from the commonly used forms of the Kozeny-Carman equation and Archie's law. However, by using the effective porosity instead of the total porosity, I find that the proposed relations for permeability and formation factor are valid and give good approximation to the experimentally observed values. The problem remains with estimating the effective porosity from the total porosity, or accurately measuring the former in situ.

ACKNOWLEDGMENTS

This work was supported by Gas Research Institute, Contract 5094-210-34125. I thank Gary Mavko, Tapan Mukerji and David Elata for helpful discussions.

REFERENCES

Berge, P.A., Berryman, J.G., and Bonner, B.P., 1993, Influence of microstructure on rock elastic properties: Geophys. Res. Lett., **20**, 2619-2622.

Bourbie, T., and Zinszner, B., 1985, Hydraulic and acoustic properties as a function of porosity in Fontainebleau sandstone: J. Geophys. Res., **90**, 11 524-11 532.

Chen, Q., 1992, Critical concentration models for the mechanical and acoustic properties of porous materials: Ph.D. dissertation, Stanford University.

Dvorkin, J., Nur, A., and Yin, H., 1994, Effective properties of cemented granular material: Mechanics of Materials, **12**, 207-217.

Dvorkin, J., and Nur, A., 1995, Elasticity of high porosity sandstones: theory for two North Sea data sets: Geophysics, **61**, 1363-1370.

Gueguen, Y., and Dienes, J., 1989, Transport properties of rocks from statistics and percolation: Math. Geol., **21**, 1-13.

Gueguen, Y., and Palciauskas, V., 1994, Introduction to the physics of rocks: Princeton University Press.

Han, D.H., 1986, Effects of porosity and clay content on acoustic properties of sandstones and unconsolidated sediments: Ph.D. thesis, Stanford University.

Hashin, Z., 1962, The elastic moduli of heterogeneous materials: J. Appl. Mech., **29**, 143-150.

Hashin, Z. and Shtrikman, S., 1963, A variational approach to the elastic behavior of multiphase materials: J. Mech. Phys. Solids, **11**, 127-140.

Jacquin, C., 1964, Correlations entre la permeabilite et les caracteristiques geometriques du gres de Fontainebleau: Rev. Inst. Fran. Petr., **19**, 921-937.

Mukerji, T., Berryman, J., Mavko, G., and Berge, P., 1995, Differential effective medium modeling of rock elastic moduli with critical porosity constraints: Geophys. Res. Lett., **22**, 555-558.

Nur, A., Marion, D., and Yin, H., 1991, Wave velocities in sediments, in Hovem, J.M., Richardson, M.D., and Stoll, R.D., Eds., Shear waves in marine sediments: Kluwer Academic Publishers.

Strandenes, S., 1991, Rock physics analysis of the Brent Group Reservoir in the Oseberg Field: Stanford Rock Physics and Borehole Geophysics Project.

Zimmerman, R.W., 1991, Compressibility of sandstones: Elsevier.

APPENDIX

COMPARING THE MUHS CURVES TO EXPERIMENTAL DATA FOR SINTERED GLASS BEADS

Figure 8 gives bulk and shear moduli versus porosity for dry sintered glass beads (Berge et al., 1993). The MUHS model predictions depart from the data. The reason is that during sintering pores in glass do not maintain their shape. Rather they gradually become rounder minimizing their specific surface area. This process acts to increase pore stiffness. The result is that the data points lie above the MUHS curves.

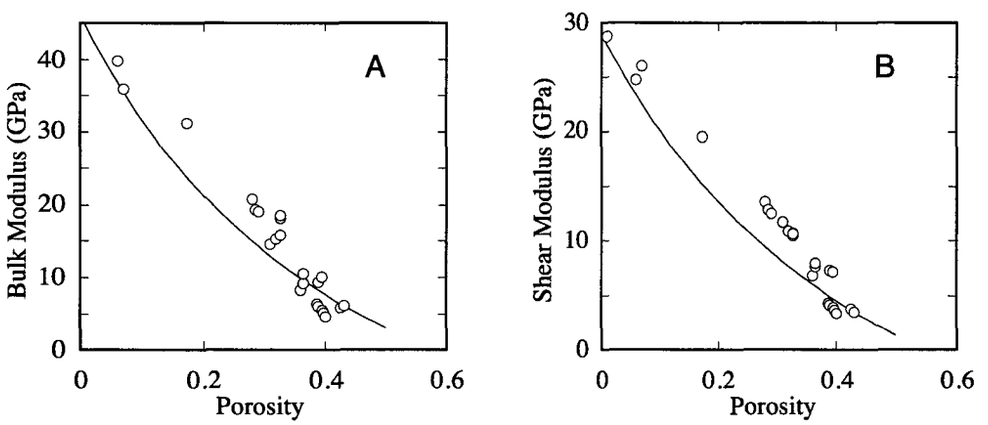

Figure 8. Elastic moduli versus porosity: data points are for sintered glass beads (Berge et al, 1993), the solid lines are the MUHS curves. a. Bulk modulus. b. Shear modulus.

CHAPTER 6

PERMEABILITY IN CLEAN AND SHALY SANDSTONES

ABSTRACT

I develop a model for single-phase fluid transport in clean and shaly sandstones. The clean sandstone model consists of a three-dimensional network of pipes of two types. One type carries flow, and represents the effective porosity, and the other, which does not carry flow, represents the trapped porosity. I consider two end-member configurations: a mixed-network, that contains both types, and a separate-network, where a pipe can connect only with others of its type. In the mixed-network, the trapped porosity causes an increase in tortuosity (and therefore lowers permeability), and in the separate network it does not. The 'real-world' analogy may be trapped porosity at pore-throats, versus bypassed porosity. The theoretical formulas, calculated for these two end-members, give very good bounds on the porosity-permeability relationship in Fontainebleau sandstone.

To estimate the permeability of shaly sandstones, I simply incorporate clay into the clean sandstone models. A high permeability estimate is calculated by assuming that clay uniformly coats each pipe in a separate-network model. A low permeability estimate is calculated by assuming that clay blocks the conducting pipes of a mixed-network model. These synthetic examples may be compared to grain-coating versus throat blocking clays in shaly sandstones. The model, which requires porosity, clay content, and grain-size as input, was tested on two independent data sets, containing seventy-two shaly sandstone samples. The measured permeability almost always fell between the calculated upper and lower estimates. I show that, for my data, the log-average of the high and low estimates is always within an order of magnitude of the measured permeability. In fact, it predicts the permeability better than the Timur equation, and the BP permeability predictor, both of which require more input. Moreover, there is a clear correlation between measured permeability and the high-permeability estimate, k_{high}. The permeabilities of sixty-eight of the seventy two samples are within an order of magnitude of $0.14k_{high}$. However, to determine the usefulness of these formulas, let alone decide if one is significantly better than another, it is necessary to test them on more data. Because the formulas I present are derived from a physical model, there is a potential for increasing their accuracy, by refining the model, or adapting it to specific types of rock.

INTRODUCTION

An important objective of rock physics is to provide reliable estimates of permeability in wells or zones where core measurements are not available. At this time there is no log which measures permeability directly, therefore it must be estimated indirectly from logs of other petrophysical parameters (for an overview, see Nelson, 1994). This is often very difficult, because permeability is critically dependent on the internal microstructure of the pore-space. Two rocks with the same porosity, clay content, and grain-size, may have orders of magnitude difference in their permeabilities. Even Fontainebleau sandstone, which is very clean and well-sorted, and is often considered an 'ideal' porous medium, shows an order of magnitude permeability scatter for a given (low to intermediate) porosity. For this reason, Fontainebleau sandstone is a good starting point for modeling, and I begin by using a three-dimensional network model, to analyze its porosity-permeability behavior. The analysis provides good upper and lower bounds on the permeability of Fontainebleau, and is then extended to include sandstones with clay, and provide high and low estimates of their permeability.

PERMEABILITY MODEL FOR CLEAN SANDSTONE

Observations show that pore-space in clean sandstones is connected even at very low porosity values (Dullien, 1992). However, some of this porosity, the trapped porosity, is very poorly connected, and does not contribute to fluid flow (see Chapter 5). The effective porosity is the complement of the trapped porosity, and it is, by definition, well-connected.

In Chapter (5) I used the following empirical formula, to fit the experimental results by Bourbie and Zinsner (1985), relating the effective to the total porosity, in Fontainebleau sandstone:

$$\phi_e = 1.3486(\phi - 0.021)^{1.4}. \tag{1}$$

Let us now consider a network of randomly oriented and distributed pipes of variable length λ , and radii r. The average distance between axes of two pipes, (which I will later assume to represent the grain size), is d and the pipes may intersect. The permeability of this network is given by (Gueguen and Dienes, 1989)

$$k = \frac{\pi}{32} f \frac{\overline{\lambda}}{d^3} \overline{r^4}, \tag{2}$$

where f is the fraction of connected pipes, and $\overline{r^4}$ is the fourth-order moment of the radius distribution. I now modify this simple network to account for free and trapped porosities. Let us assume the pipes can be separated into two types: effective pipes that allow free flow -- representing the effective porosity, and trapped pipes that do not allow flow -- representing the trapped porosity. For simplicity, I also assume that they all have the same length, although retaining variability is not going to affect the end result, and that other parameters are uniform within each class. If these two classes of pipes are homogeneously distributed within the same network, then Equation (2) can be re-written:

$$k = \frac{\pi}{32}\frac{\lambda}{d^3}\frac{\phi_e}{\phi}r_e^4, \tag{3}$$

where the subscript e refers to the effective porosity class of pipes, and ϕ is the total porosity. Applying the concept of uniform porosity reduction (UPR) introduced in the previous chapter, Equation (3) leads to the following relationship:

$$k \propto \frac{\phi_e^3}{\phi} \tag{4}$$

To eliminate the proportionality in Equation (4), we can use a reference sample from the data set, whose parameters we denote with the subscript 0, and obtain

$$k = k_0 \frac{d^2}{d_0^2}\frac{\phi_e^3\phi_0}{\phi_{0e}^3\phi}. \tag{5}$$

The subscript e denotes that Equation (1) was applied to the parameter that precedes it. If, on the other hand, the two classes of pipes remain separate, then Equation (2) leads to

$$k = \frac{\pi}{32}\frac{\overline{\lambda}}{d^3}\overline{r_e^4}. \tag{6}$$

Again, if we apply UPR, we find that

$$k \propto \phi_e^2. \tag{7}$$

The last relation is similar to the one derived for a one-dimensional permeability model in the previous chapter, and can also be calibrated, using a reference sample, to give

$$k = k_0 \frac{d^2}{d_0^2} \frac{\phi_e^2}{\phi_{0e}^2}. \tag{8}$$

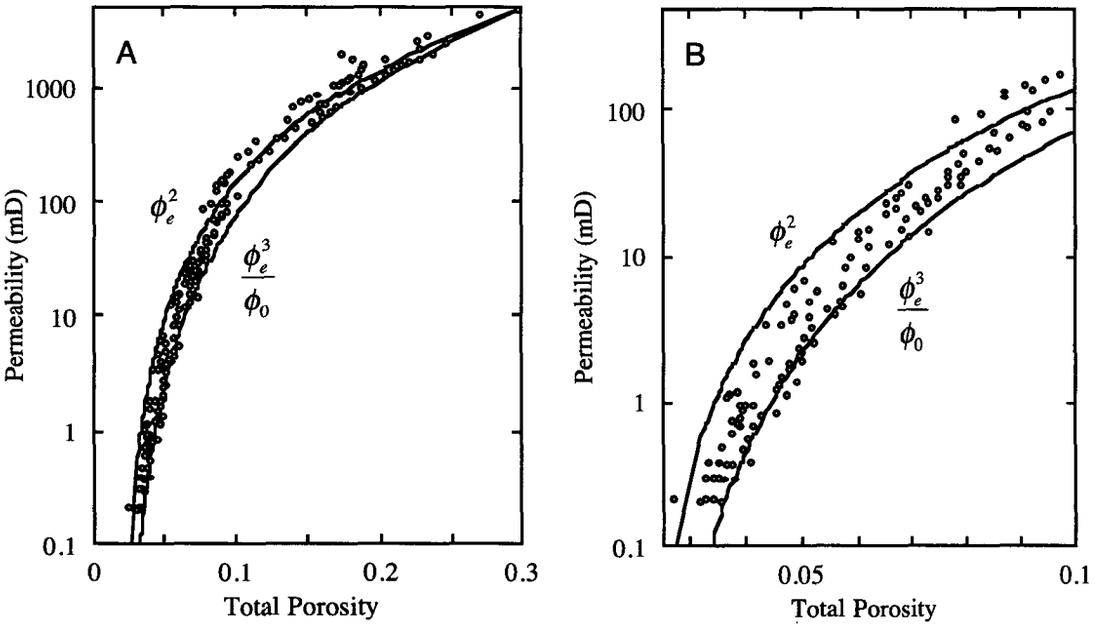

Figure 1: Equations (5) and (8) are compared to experimental data acquired by Bourbie and Zinsner (1985), **a**. over the full porosity range, and **b**. for the low-porosity samples. The mixed-network end-member provides a high bound for most of the data, and the separate-networks end-member provides a low bound.

In Figures (1a) and (1b), I compare Fontainebleau sandstone permeability data (Bourbie and Zinsner, 1985), to Equations (5) and (8). The equations were calibrated using the highest-porosity sample in the set ($\phi = 0.29833, k = 4771.6mD$). The mixed-network end-member (Equation 5), provides a low bound for the data, and the separate-networks end-member (Equation 8) provides an upper bound. An interpretation of these

results, is that the trapped porosity can affect the permeability differently, depending on the manner of its distribution in the pore-space. When it is incorporated into the conducting network (e.g., as pore throats), it increases the tortuosity of the network, whereas if it remains separate (e.g., bypassed porosity), the tortuosity is not affected. These two end-member networks will be used in the next section as reference networks for modeling the permeability of shaly sandstones.

PERMEABILITY MODEL FOR SHALY SANDSTONES

In this section, I model permeability in shaly sandstones, by incorporating clay into the networks developed for clean sandstones. This model is obviously a very simplified one since, in nature, sandstones with the same bulk properties may show great variability in microstructure. Keeping this limitation in mind, the model will still prove useful and instructive.

To obtain a high estimate for the permeability of a shaly sandstone, let us consider the separate-networks end-member, and assume that clay uniformly coats the inside of all pipes (Figure 2a). If the measured porosity and clay content are, respectively, ϕ and C, and the micro-porosity of the clay is ϕ_c, then the macro-porosity of the network is simply $\phi - C\phi_c$. The uniform clay coating reduces the pipe cross-sections proportionately, therefore, Equation (1) can be used to calculate the fraction of the macro-porosity that carries Poiseuille flow, i.e., the effective macro-porosity. Adjusting Equation (8), we find that,

$$k_{high} = k_0 \left[\frac{d(\phi - C\phi_c)_e}{d_0 \phi_{0e}} \right]^2 + k_c C. \tag{9}$$

The low permeability estimate is obtained by putting the clay, in each effective pipe of the mixed-network end-member, perpendicular to the flow (Figure 2b). Adjusting Equation (5), we obtain

$$\frac{1}{k_{low}} = \frac{\phi + \phi_c C}{(\phi + \phi_c C)_e^4} \left(\frac{(\phi + \phi_c C)_e - C}{k_0 (d/d_0 \phi_{0e})^2} + \frac{(\phi + \phi_c C)_e C}{k_c} \right). \tag{10}$$

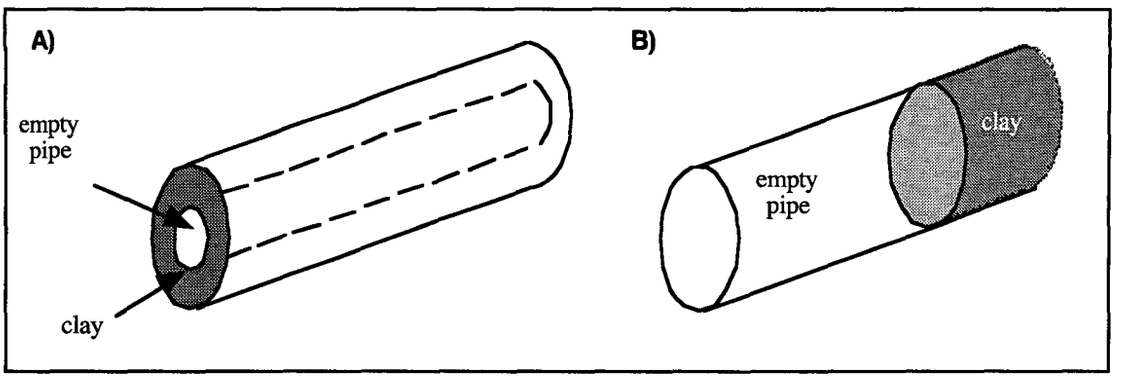

Figure 2: Representative effective pipes from the two end-member network configurations: **a**. high permeability, and **b**. low permeability. The empty portion of the pipes allows Poiseuille flow.

RESULTS

The model was tested on seventy-two sandstone samples from two different data sets. The first data set (thirty-four samples) was compiled from the Catalog of Geological and Engineering Properties for Sandstones (1987), and the second (thirty-eight samples), from experimental results published by Klimentos and McCann (1990). The sandstones in these data sets cover a very wide range of porosities, permeabilities, compositions, and structures. Some are tight-gas sandstones, others may be glauconitic, carbonate-cemented, micaceous, and so on. In Figure (3), I plot the calculated high and low estimates, versus the measured permeability. In Figures (4a) and (4b), I plot the measured permeability, and the high and low estimates, versus the porosity.

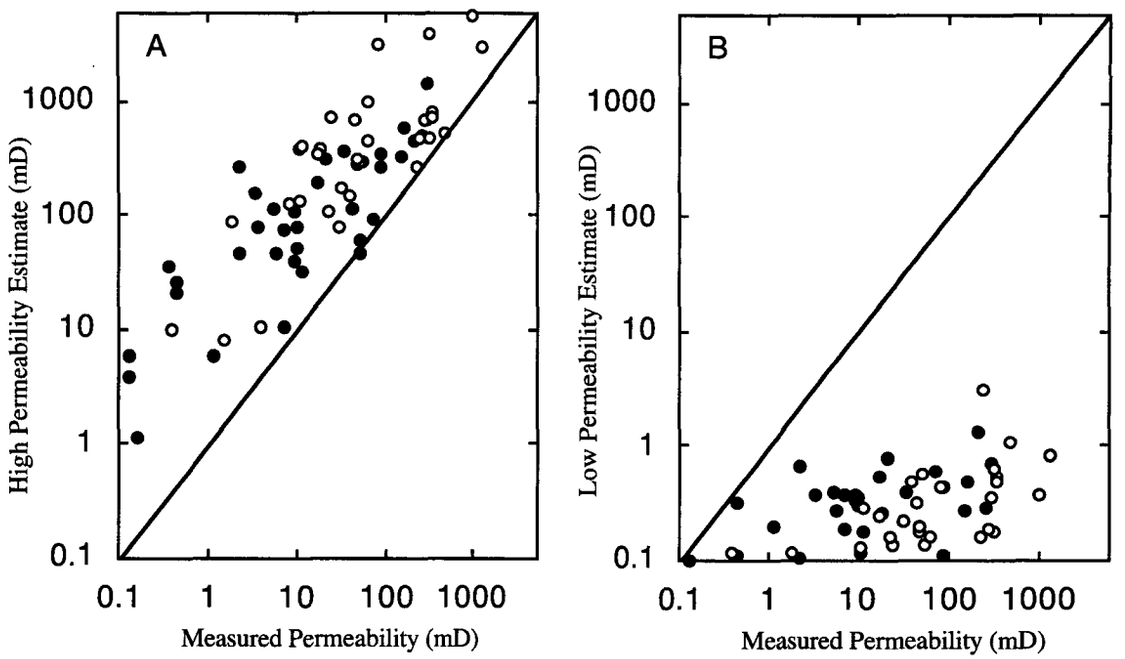

Figure 3: High (**a**) and low (**b**) permeability estimates, versus measured permeabilities, for the Rock Catalog data set (empty circles), and for the Klimentos and McCann data set (filled circles). The data almost always lies between these estimates.

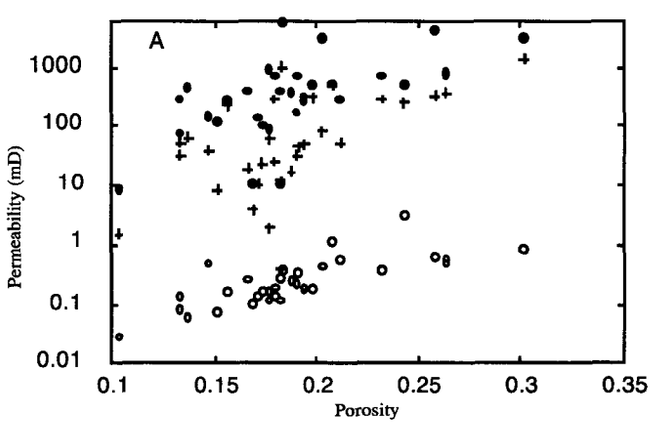

Figure 4a: High and low estimates on the permeabilities of the sandstones from the Rock Catalog data set. Almost all the measured permeabilities (crosses), are between the high (filled circles) and low (open circles) permeability estimates.

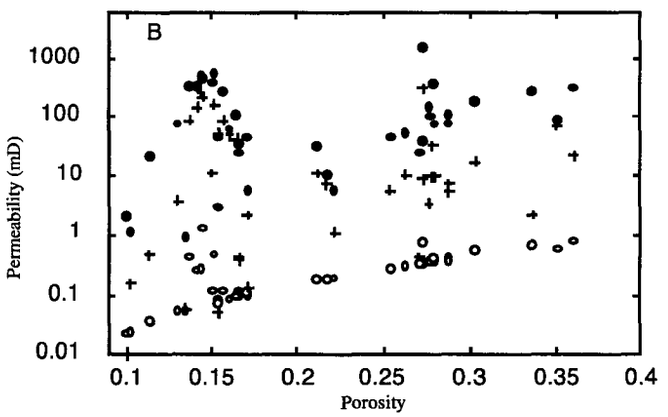

Figure 4b: High and low estimates on the permeabilities of the sandstones from the Klimentos and McCann data set. Almost all measured permeabilities (crosses), are between the high (filled circles) and low (open circles) permeability estimates.

As expected, almost every data point falls between its corresponding high and low estimates. Furthermore, we can see that many characteristics of the real data cloud, are mimicked to some by the calculated synthetic data clouds. This is very apparent in the high permeability estimates, especially for the Klimentos and McCann data set (Figure 4b). In fact, for all samples but one, the permeability is within an order of magnitude of $0.14k_{high}$. This indicates that the model captures some aspects of permeability in real sandstones. To test the usefulness of the model, I used the log-average of the high and low estimates, to calculate the permeabilities of the samples in the Rock Catalog data base, and compared the results to those obtained by using two well established permeability estimators: Timur's equation (Figure 5a), and the BP permeability predictor (Figure 5b). These methods need additional input, (e.g., Timur's equation requires the irreducible water saturation, and the B.P. predictor requires grain-size distribution), none the less, the log average predicted the permeabilities of the sandstones somewhat more accurately. The difference, however, is small, and the equations should be compared over a much wider data base.

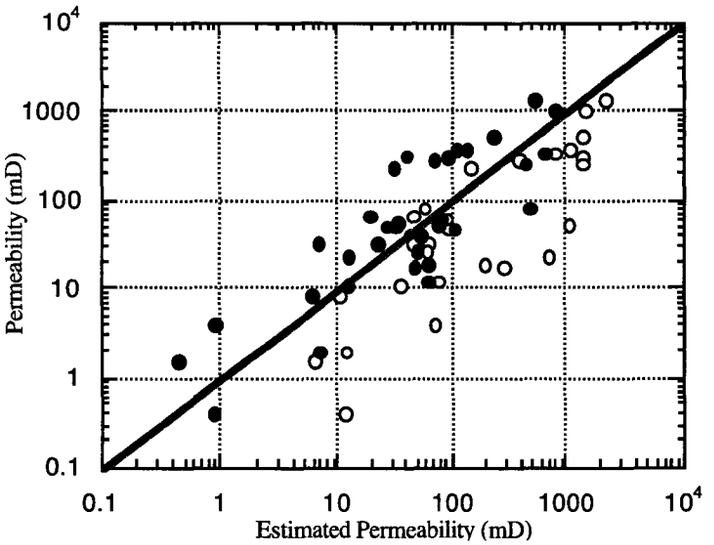

Figure 5a: Permeabilities were calculated using the Timur equation (open circles), and using the log-average of the high and low permeability estimates (Equations 9 and 10, respectively), for the same data set (Rock Catalog). These estimates are plotted versus the measured permeabilities. The log-average gives a slightly better estimate.

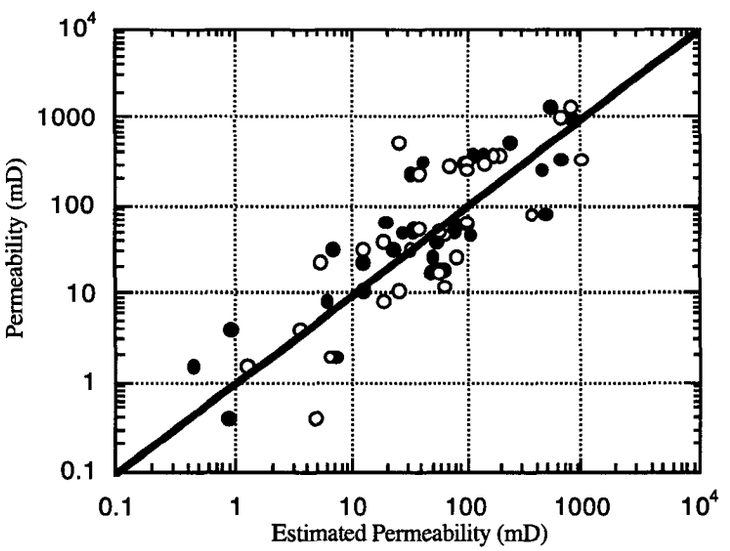

Figure 5b: Permeabilities were calculated using the BP Predictor (open circles), and using the log-average of the high and low permeability estimates (Equations 9 and 10, respectively), for the same data set (Rock Catalog). These estimates are plotted versus the measured permeabilities. Again, the log-average gives a slightly better estimate.

CONCLUSIONS

The clean sandstone model I presented, reproduces the main features of the porosity-permeability relation in Fontainebleau sandstone: the general trend, and the characteristic scatter. The model suggests that this scatter results from an increasing variability in the tortuosity, at intermediate and low porosities. As the total porosity decreases, an increasing fraction becomes 'trapped', i.e., it does not allow flow. The porosity-permeability scatter reflects the variable effect this trapped porosity has on the flow, depending on where it is located (e.g., pore throats, versus by-passed porosity).

The analysis was then extended to include sandstones with clay. I used two end-member configurations of the network model to provide high and low permeability estimates. The model, which requires as input, porosity, clay content, and grain-size, was tested on two independent data sets, containing seventy-two Shaly sandstone samples. The measured permeability almost always fell between the calculated high and low estimates. For the data analyzed, the log-average of the high and low estimates is always within an order of magnitude of the measured permeability. In fact, it predicts the permeability better than the Timur equation, and probably better than the BP permeability predictor, both of which require more input. Moreover, there is a clear correlation between measured permeability and the high-permeability estimate, k_{high}. The permeability of sixty-eight of the seventy two samples are within an order of magnitude of $0.14k_{high}$.

Because the formulas I present are derived from a physical model, there is a potential for improving them, by refining the model, or adapting it to specific situations. For example, the model consistently over-estimates the permeability of sandstones with a high fraction of micro-porous chert. If, in this case, I add this micro-porosity to the clay micro-porosity, the calculated effective porosity decreases, and the model yields a more realistic estimate of the permeability

ACKNOWLEDGMENTS

Amos Nur and Jack Dvorkin collaborated with me on this work, that was supported by the SRB.

REFERENCES

Bourbie, T., and Zinsner, B., 1985, Hydraulic and acoustic properties as a function of porosity in Fontainebleau sandstone: JGR, **90**, no. B13, 11524-11532.

Dullien, F.A.L., 1992, Porous media, fluid transport, and pore structure: Academic Press, Inc.

Gueguen, Y., and Dienes, J., 1989, Transport properties of rocks from statistics and percolation: Mathematical Geology, **21**, no. 1, 1-13.

Klimentos, T., and McCann, C., 1990, Relationships among compressional wave attenuation, porosity, clay content, and permeability in sandstones: Geophysics, **55**, no. 8, 998-1014.

Nelson, P.H., 1994, Permeability-porosity relationships in sedimentary rocks: The Log Analyst, **35**, no. 3, 38-62.

Pickell, J.J., Swanson, B.F., and Hickman, W.B., 1966, Application of air-mercury and oil-air capillary pressure data in the study of pore structure and fluid distribution: SPE Journal, 55-61.

Reservoirs, Inc., and Robert M. Sneider Exploration, Inc., 1987, A catalog of geological and engineering properties for sandstones: Copyright by Reservoirs Inc.

Timur, A., 1968, An investigation of permeability, porosity, and residual water saturation relationships for sandstone reservoirs: The Log Analyst, **9**, no. 4, 8-17.

CHAPTER 7

STRESSES IN ANISOTROPIC CYLINDERS

INTRODUCTION

Axisymmetrical stresses in an infinitely long hollow isotropic circular cylinder (plane strain) quickly approach their asymptotic values as the external radius increases. This is not the case if the cylinder is even slightly anisotropic -- asymptotic solutions (for an infinitely large external radius) do not exist. I find the mechanical meaning of this disparity by using formulas for radial and hoop stresses in a cylindrically anisotropic cylinder with constant finite stresses at the boundaries: (a) The internal stresses increase infinitely with increasing external radius, if the cylinder is stiffer in the radial direction than in the tangential direction. (b) At any fixed point inside the cylinder, the stresses approach zero as the outer radius increases, if the cylinder is stiffer in the tangential direction than in the radial direction. I call the former effect "stress amplification", and the latter one "stress shielding". Both effects are closely related to the decay of boundary conditions and, in general, to the problem of applicability of Saint-Venant's principle to anisotropic solids.

ANALYSIS

Stresses in an isotropic plane with a circular hole (plane strain) and uniform axisymmetrical far-field stresses can be calculated as asymptotes of those in a thick-walled cylinder with an external radius approaching infinity. However, such asymptotic values do not exist if the cylinder has even slight cylindrical anisotropy. Apparently, this qualitative observation is closely linked to the quantitative problem of decay of boundary conditions in anisotropic elasticity (e.g., Knowles and Horgan, 1969; Horgan, 1974) and, more generally, to the issue of applicability of Saint-Venant's principle to anisotropic bodies. Comprehensive reviews of the latter problem can be found in Horgan and Knowles (1983), Horgan (1989), and Horgan and Simmonds (1994).

Consider an infinitely long linearly-elastic cylinder with cylindrical anisotropy. Both the generator of the cylinder and the axis of anisotropy lie along the z-axis of a cylindrical coordinate system (r,θ,z). Normal stress component in the z direction is zero, the pressure inside the cylinder is zero, and the outside pressure P is constant. Hooke's law that is appropriate for this problem is (Lekhnitskii, 1963):

$$e_{rr} = \frac{1}{E_r}\sigma_{rr} - \frac{\nu_{\theta r}}{E_\theta}\sigma_{\theta\theta}, \quad e_{\theta\theta} = \frac{1}{E_\theta}\sigma_{\theta\theta} - \frac{\nu_{r\theta}}{E_r}\sigma_{rr}, \tag{1}$$

where σ_{rr}, $\sigma_{\theta\theta}$, e_{rr}, and $e_{\theta\theta}$ are stress and strain components, E_r and E_θ are Young's moduli in the r and θ directions, respectively, and $\nu_{\theta r}$ and $\nu_{r\theta}$ are the appropriate Poisson's ratios. By using equations (1) together with the equations of equilibrium, one can arrive at the following formulas for the radial (σ_{rr}) and hoop ($\sigma_{\theta\theta}$) stresses:

$$\begin{aligned}
\sigma_{rr} &= -\frac{Pb^{n+1}}{b^{2n} - a^{2n}}\left(r^{n-1} - a^{2n}r^{-n-1}\right), \\
\sigma_{\theta\theta} &= -\frac{nPb^{n+1}}{b^{2n} - a^{2n}}\left(r^{n-1} + a^{2n}r^{-n-1}\right), \\
n &= \sqrt{\frac{E_\theta}{E_r}},
\end{aligned} \tag{2}$$

where a and b are the internal and external radii of the cylinder, respectively. These formulas are similar to those given by Lekhnitskii (1963). In the isotropic case where $n = 1$, equation (2) reduces to the standard solution

$$\sigma_{rr} = -\frac{Pb^2}{b^2 - a^2}\left(1 - \frac{a^2}{r^2}\right), \sigma_{\theta\theta} = -\frac{Pb^2}{b^2 - a^2}\left(1 + \frac{a^2}{r^2}\right). \tag{3}$$

Equation (3) yields for $b >> a$:

$$\sigma_{rr} = -P\left(1 - \frac{a^2}{r^2}\right), \sigma_{\theta\theta} = -P\left(1 + \frac{a^2}{r^2}\right). \tag{4}$$

By plotting the stresses as given by equation (3) versus the radial coordinate (Figure 1), it is observed that stress distribution curves in a finite-thickness cylinder gradually converge to the asymptotic (infinite external radius) solution as given by equation (4).

However, equations (2), where $n \neq 1$, do not allow one to obtain an asymptotic formula for an infinite-thickness cylinder. Physically, this result means that both radial and hoop stress distributions in anisotropic cylinders do not converge to asymptotic curves as the thickness of the cylinders increases. If $n > 1$ (Figure 2) the influence of the stress at the external boundary decays much faster than in the isotropic case. I call this effect stress

shielding: At any fixed point inside the cylinder, the stresses approach zero as the outer radius increases. If $n < 1$, we get the opposite effect -- the external boundary condition affects the inside stresses stronger than it does in the isotropic case. This results in stress concentrations near the inner radius that are larger than in the isotropic case. These stresses will increase infinitely with the increasing outer radius (Figure 3). I call this effect stress amplification.

Radial and hoop stresses in cylinders of fixed radii are plotted in Figure 4 for isotropic and anisotropic cases. Again, if $n > 1$, stresses near the internal radius are smaller than in the isotropic case (shielding). If $n < 1$, these stresses are larger than in the isotropic case (amplification).

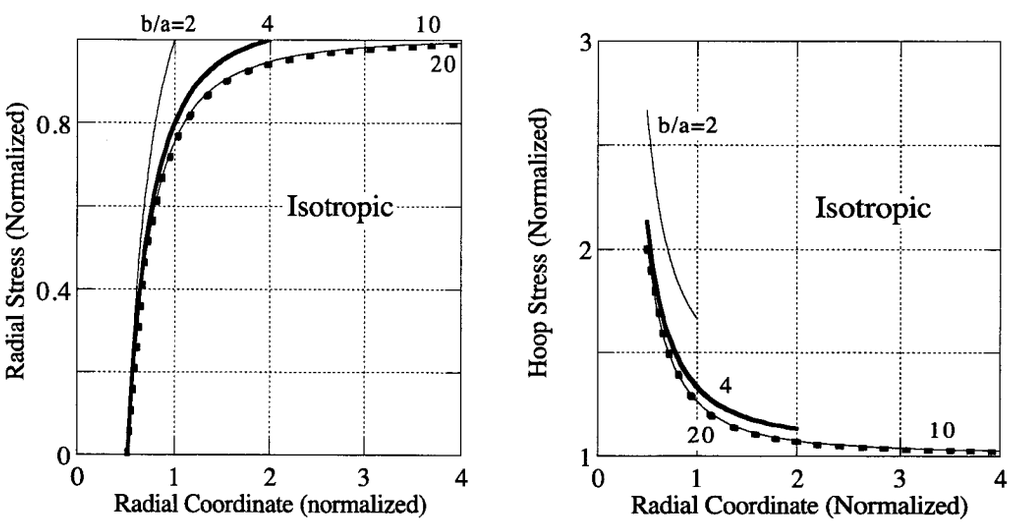

Figure 1: Radial (left) and hoop (right) stresses versus the radial coordinate in isotropic cylinders of varying thickness. The stresses are normalized by the external pressure, and the radial coordinate is normalized by the internal diameter.

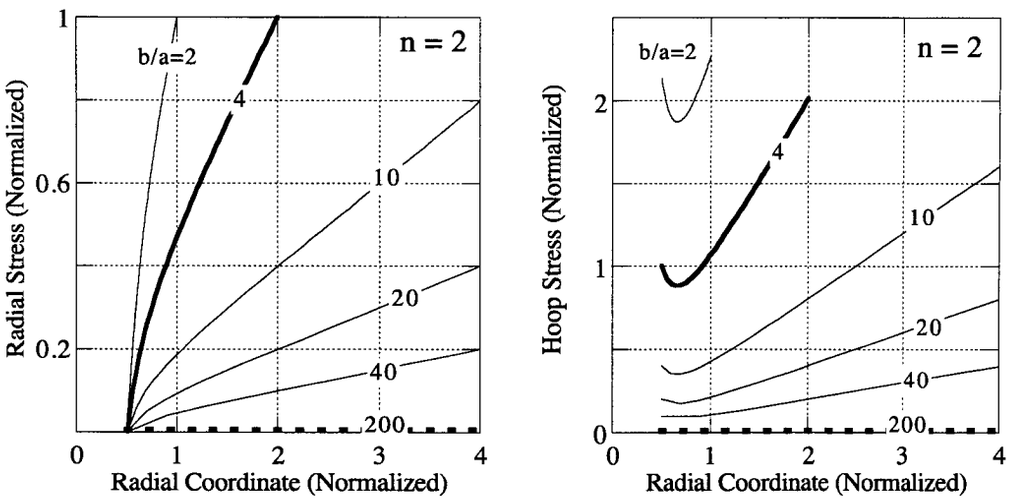

Figure 2: Radial (left) and hoop (right) stresses versus the radial coordinate in anisotropic ($n > 1$) cylinders of varying thickness. The stresses are normalized by the external pressure, and the radial coordinate is normalized by the internal diameter.

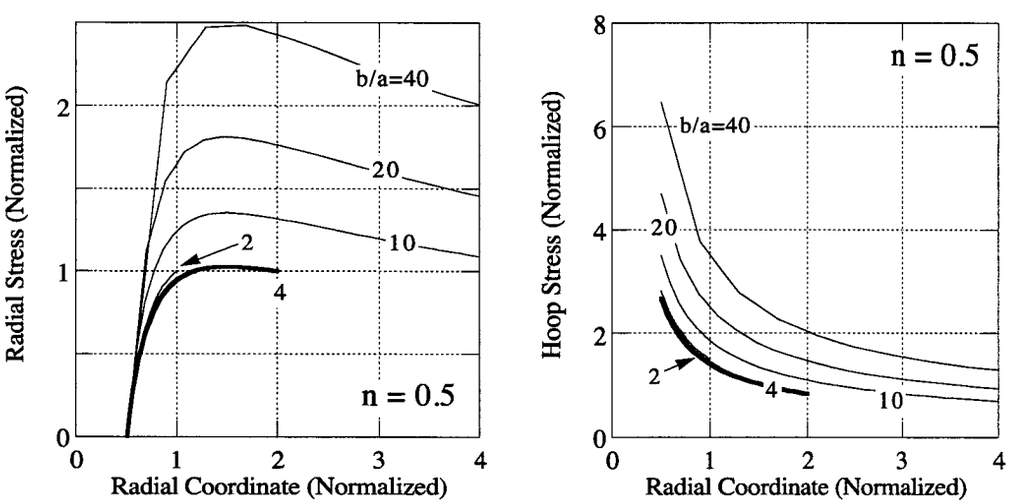

Figure 3: Radial (left) and hoop (right) stresses versus the radial coordinate in anisotropic ($n < 1$) cylinders of varying thickness. The stresses are normalized by the external pressure, and the radial coordinate is normalized by the internal diameter.

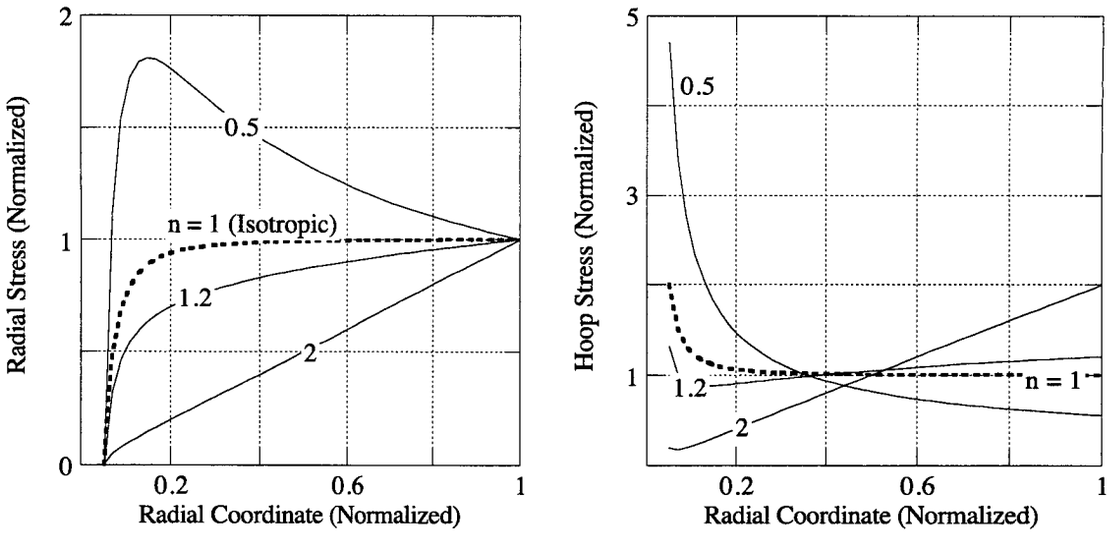

Figure 4: Radial (left) and hoop (right) stresses versus the radial coordinate in anisotropic cylinders of constant radius and varying parameter n. The stresses are normalized by the external pressure, and the radial coordinate is normalized by the internal diameter.

Both the stress shielding and the stress amplification effects can be clearly demonstrated on a simple mechanical system (Figure 5, left). This axisymmetrical system includes identical radial springs with stiffness E_r (per unit length). The radial springs are connected by two concentric hoops of tangential springs of stiffness E_θ. The radius of the external hoop is b and the radius of the internal hoop is a. The central angle between two adjacent radial springs is θ. A compressive radial force P is acting in the radial direction at every node of the external ring (Figure 5, right).

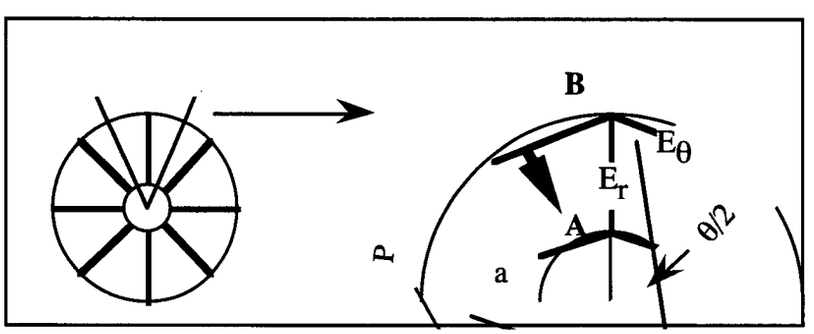

Figure 5: A simple spring model of an anisotropic ring consisting of radial springs of stiffness E_r and two hoops of tangential springs of stiffness E_θ. The force balance at nodes A and B is used to calculate the stresses in all components of the model.

By considering force balance at two nodes, A and B (Figure 5, right), we find that

$$\frac{\sigma_\theta^1}{\sigma_r} = \frac{q + n\sin\theta(1-q)}{\sin\theta}, \quad \frac{\sigma_\theta^1}{\sigma_\theta^2} = q + n\sin\theta(1-q), \tag{5}$$

where σ_r is the force in the radial springs, σ_θ^1 and σ_θ^2 are the forces in the external and internal rings, respectively, $n = E_\theta / E_r$, and $q = a/b$.

Consider an extreme case b>>a. If $n << 1$ then from equations (5) $\sigma_r >> \sigma_\theta^1$ and $\sigma_\theta^2 >> \sigma_\theta^1$. Therefore we have stress amplification near the center of the system. If $n >> 1$, equations (5) yield $\sigma_\theta^1 >> \sigma_r$ and $\sigma_\theta^1 >> \sigma_\theta^2$. In this case we have stresses near the center of the system shielded by the stiff external hoop.

ACKNOWLEDGMENTS

Jack Dvorkin collaborated with me on this work, that was supported by SRB.

REFERENCES

Knowles, J.K., and Horgan, C.O., 1969, Int. J. Solids Structures, **5**, 33.

Horgan, C.O., 1974, Int. J. Solids Structures, **10**, 837.

Horgan, C.O., and Knowles, J.K., 1983, Advances in Applied Mechanics, **23**, 179.

Horgan, C.O., and Simmonds, J.G., 1994, Composites Engineering, **3**, 279.

Lekhnitskii, S. G., 1981, Theory of elasticity of an anisotropic elastic body, Mir, Moscow.

APPENDIX

Simulation Results

Simulation 1

The rock on both sides of the interface is assumed to have the same solubility and elastic moduli. The surface energy density is $\gamma = 0.5J/m^2$.

Simulation 2

The rock on both sides of the interface is assumed to have the same solubility and elastic moduli. The surface energy density is zero.

Simulation 3

The rock on both sides of the interface is assumed to have the same elastic moduli. The lighter rock is slightly less soluble. The surface energy density is $\gamma = 0.5J/m^2$.

Simulation 1

The rock on both sides of the interface is assumed to have the same solubility. The lighter rock is more compressible. The surface energy density is $\gamma = 0.5J/m^2$.

Simulation 1: Rock on both sides has the same properties

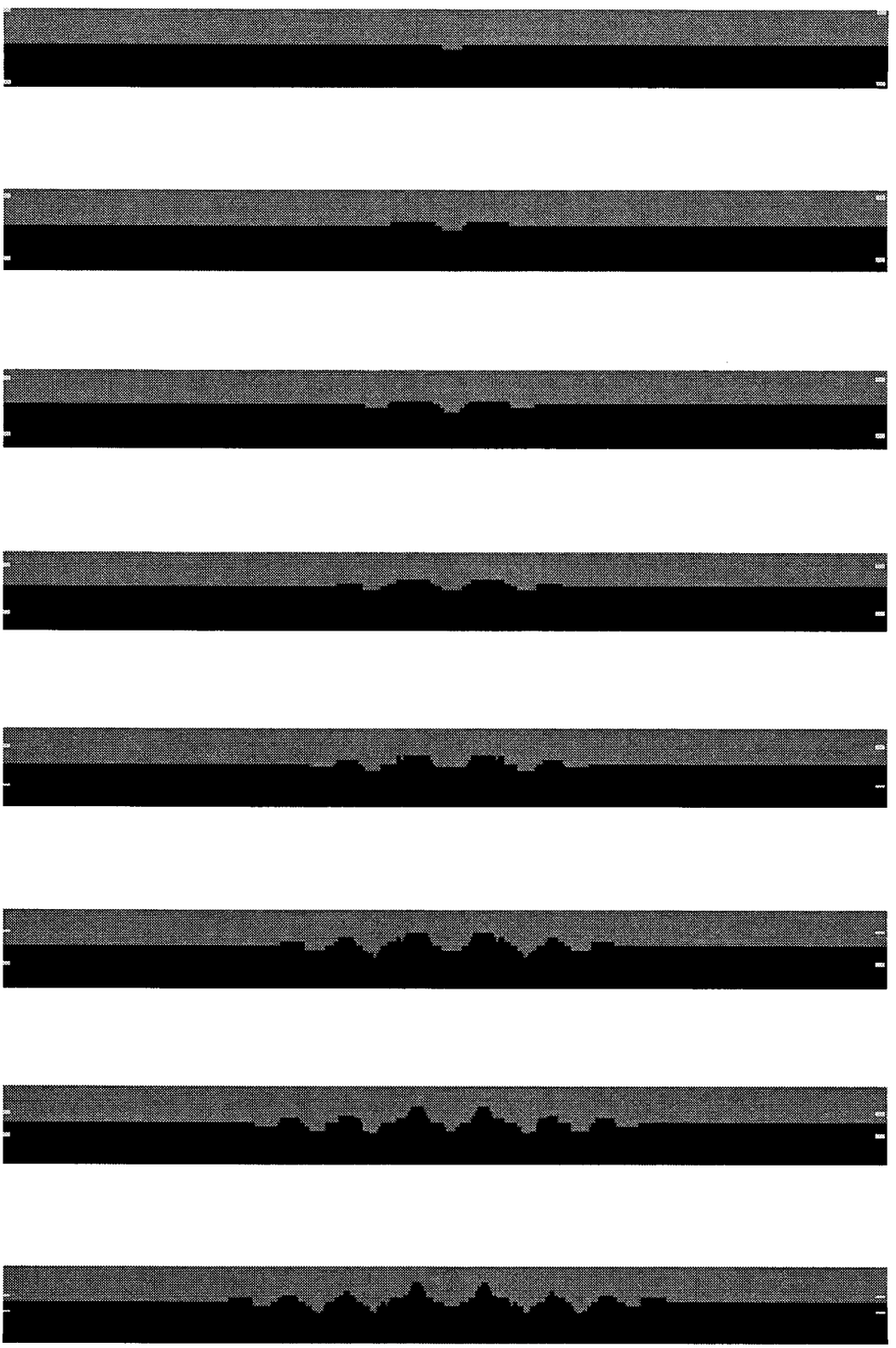

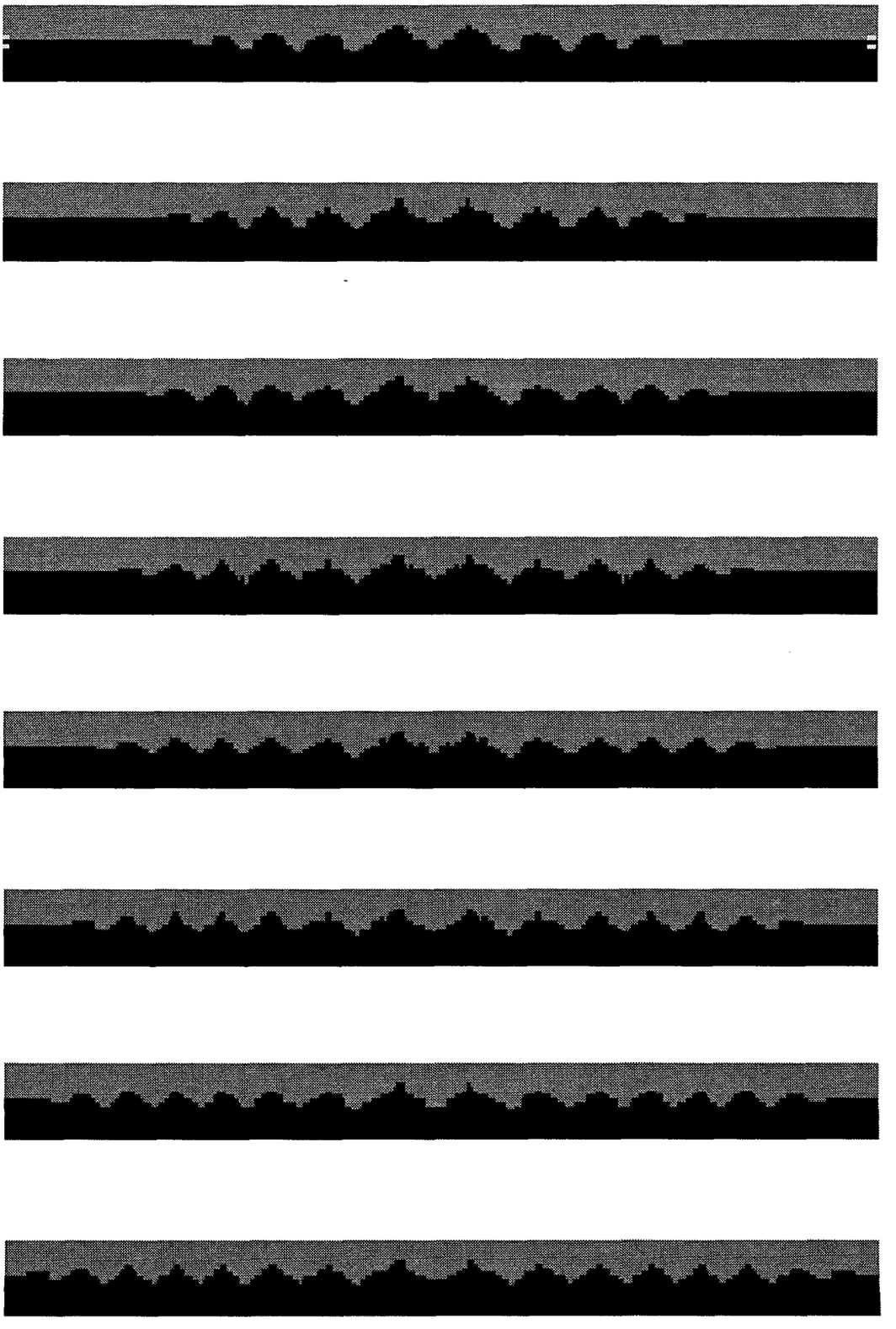

Simulation 2: Zero surface energy

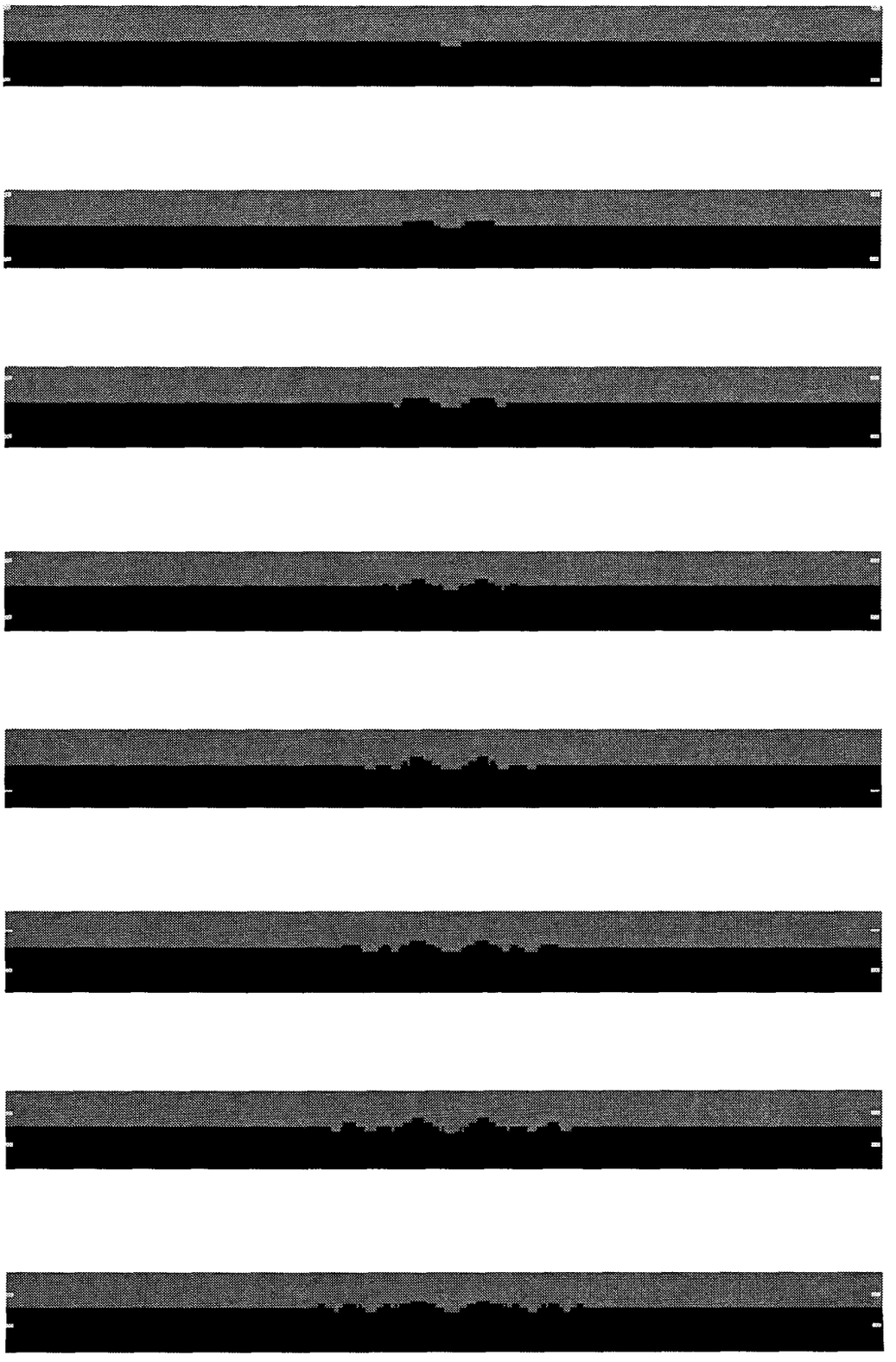

Simulation 3: Different solubilities

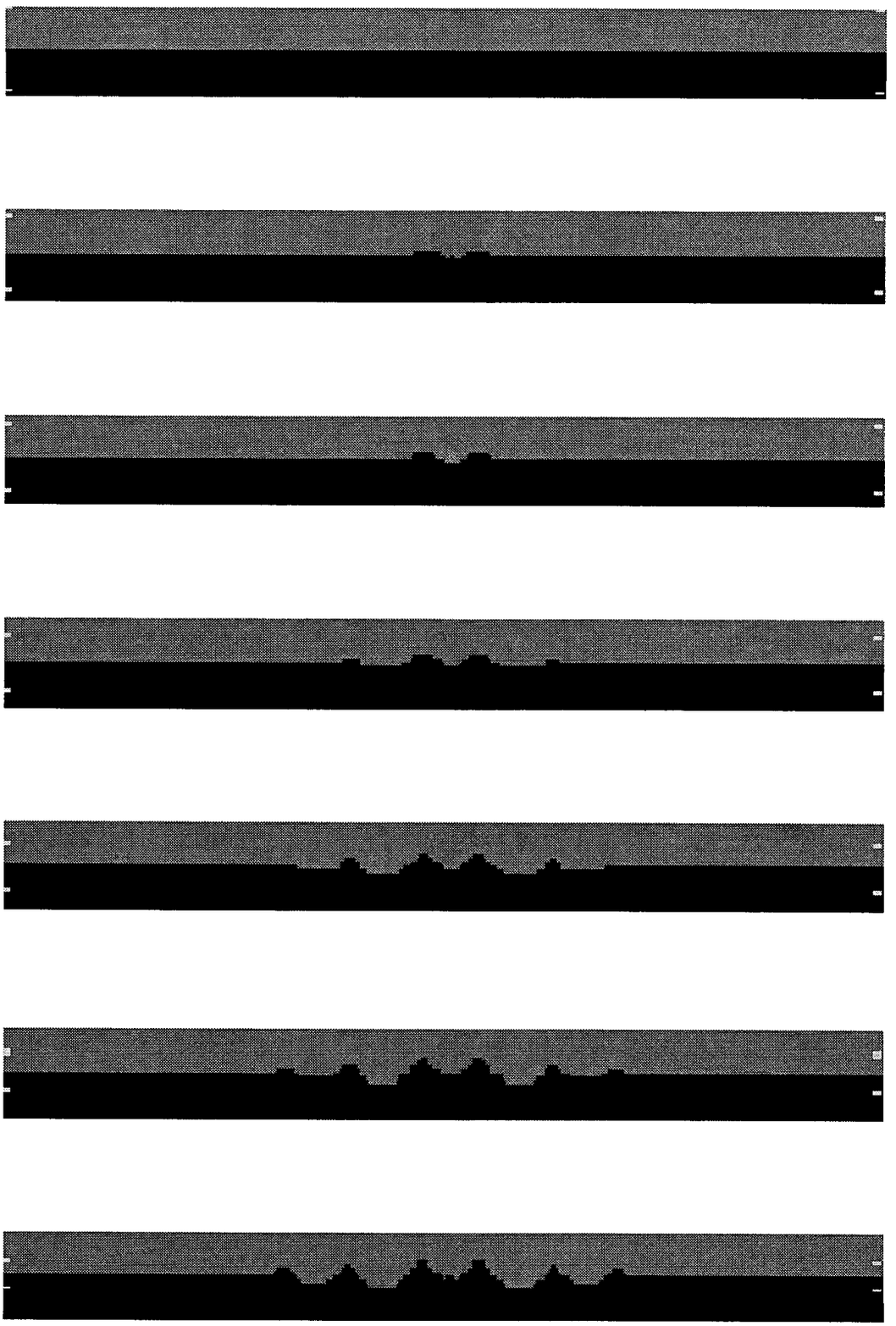

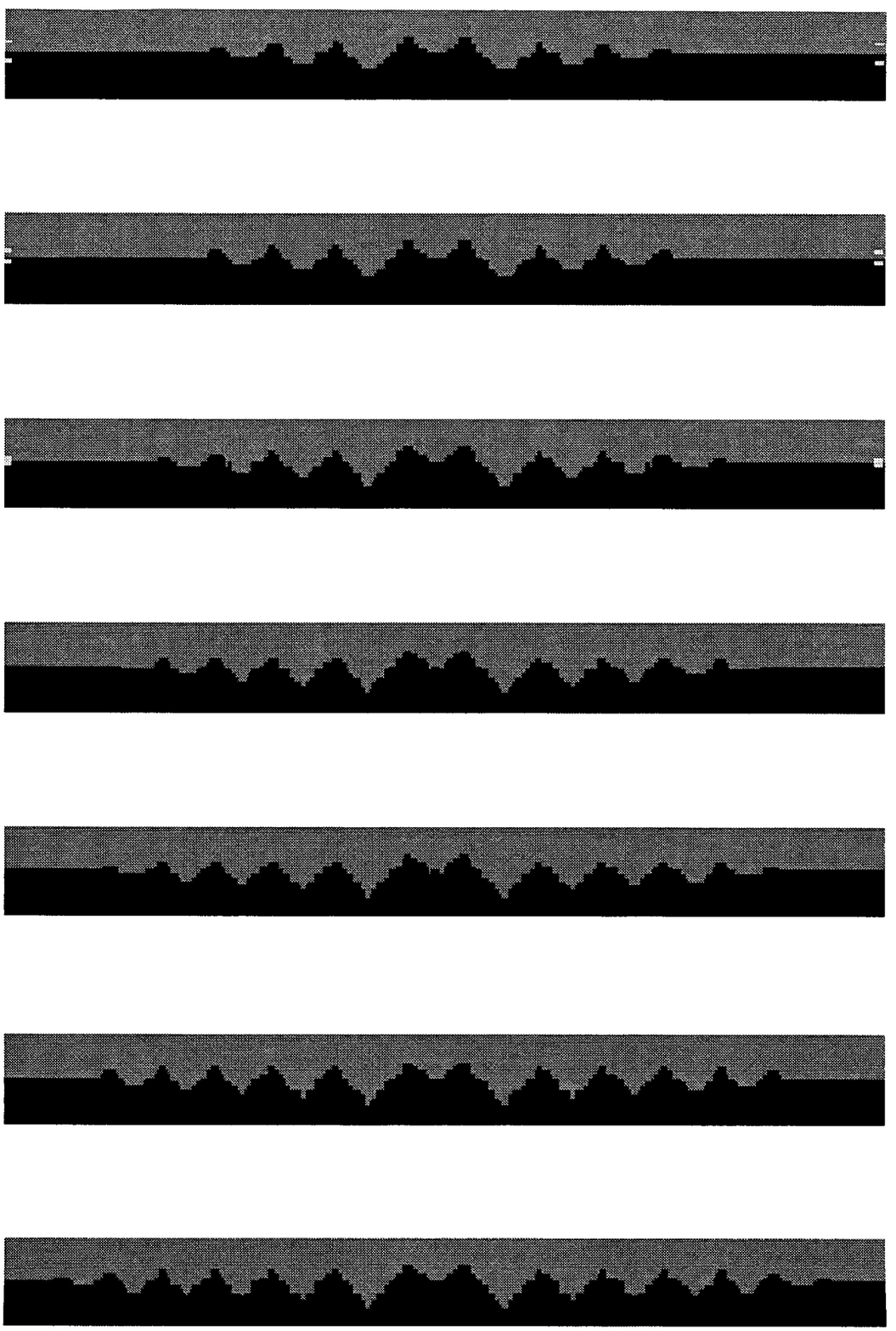

Simulation 4: Different elastic moduli